J. Fluid Mech. (2014), *vol.* 757, *pp.* 613–648.
doi:10.1017/jfm.2014.508

Stability of flow in a channel with longitudinal grooves

H. V. Moradi[1],† **and J. M. Floryan**[1]

[1]Department of Mechanical and Materials Engineering, The University of Western Ontario, London, Ontario, N6A 5B9, Canada

(Received 10 March 2014; revised 20 June 2014; accepted 28 August 2014; first published online 25 September 2014)

The travelling wave instability in a channel with small-amplitude longitudinal grooves of arbitrary shape has been studied. The disturbance velocity field is always three-dimensional with disturbances which connect to the two-dimensional waves in the limit of zero groove amplitude playing the critical role. The presence of grooves destabilizes the flow if the groove wavenumber β is larger than $\beta_{tran} \approx 4.22$, but stabilizes the flow for smaller β. It has been found that β_{tran} does not depend on the groove amplitude. The dependence of the critical Reynolds number on the groove amplitude and wavenumber has been determined. Special attention has been paid to the drag-reducing long-wavelength grooves, including the optimal grooves. It has been demonstrated that such grooves slightly increase the critical Reynolds number, i.e. such grooves do not cause an early breakdown into turbulence.

Key words: drag reduction, flow control, instability control

1. Introduction

It has been known since the original work of Reynolds (1883) that surface roughness plays an important role in the laminar–turbulent transition. This problem has most often been studied in the context of the identification of conditions when the presence of roughness can be ignored, i.e. when the wall can be viewed as hydraulically smooth. A similar question for turbulent flows, but posed in the context of drag determination, has been studied starting with Hagen (1854) and Darcy (1857); excellent reviews have been given by Jimenez (2004) and Herwig, Gloss & Wenterodt (2008).

The analysis of roughness effects must begin with modelling the wall geometry. There is an uncountable number of possible roughness forms and even the term 'roughness' is not well defined; it only means that the wall is not smooth. It might therefore be more instructive to carry out the discussion by referring to the effects of surface roughness as the effects of surface topography. Typical experimental investigations use artificially altered surface topographies (artificially created roughness forms), e.g. sets of cones, spheres, prisms, parallelepipeds, etc., with different spatial distributions (Schlichting 1979). Sand paper with various grain sizes is an especially popular roughness representation due to the belief that it accounts for the randomness

† Email address for correspondence: hvafadar@uwo.ca

of roughness forms. The most common measure of topographic features (roughness properties) is the equivalent sand roughness (Moody & Princeton 1944); see Herwig *et al.* (2008) for recent extensions of this concept. The most effective method for the theoretical modelling of surface topography relies on the reduced geometry model (Floryan 1997). The global geometric properties are extracted using projection of the surface geometry onto a convenient functional space, e.g. Fourier space, with the expectation that only a few leading Fourier modes from the Fourier expansion representing the surface topography matter. This technique permits the identification of the features of the topography that have a decisive influence on the flow response, with irrelevant geometric details removed from consideration so they do not mask the essential mechanisms. Indeed, it has been demonstrated that, in many instances, it is sufficient to use only the leading Fourier mode to capture the main physical processes with accuracy sufficient for most applications (Floryan 2007).

Use of the reduced geometry model leads to the need for the determination of the basic state as well as the disturbance field in irregular domains bounded by walls with shapes expressed in terms of arbitrary Fourier expansions. A systematic analysis of a large number of configurations is possible using either the immersed boundary conditions method (IBC) (Szumbarski & Floryan 1999; Husain, Floryan & Szumbarski 2009; Husain & Floryan 2010; Mohammadi & Floryan 2012; Moradi & Floryan 2012) or the domain transformation method (DT) (Husain & Floryan 2010; Mohammadi & Floryan 2012). Both techniques permit the determination of the flow details with spectral accuracy for the complete range of topographies of practical interest and a seamless transition between different topographic forms. Methods based on the domain perturbation have limited applicability and are unsuitable for this class of problems (Cabal, Szumbarski & Floryan 2001).

There is a large amount of experimental data dealing with the effects of surface topography (roughness) on the laminar–turbulent transition (Schlichting 1979). A frequently used criterion (Morkovin 1990) for the determination of the critical roughness size states that the roughness Reynolds number $Re_k = U_k k/\nu < 25$ for the roughness to be active, where U_k is the undisturbed velocity at height k. This criterion does not provide any insight into the flow mechanics and is unable to deal with so-called distributed surface roughness. A more fundamental understanding of the mechanics of the flow response has been achieved only recently (Floryan 2007) and has led to the formulation of a formal criterion for hydraulic smoothness. This criterion states that the surface topography is hydraulically active only when it is able to induce flow bifurcation (Floryan 2007) and the relevant critical conditions can be identified using linear stability theory. The existing analyses have been focused on two-dimensional (independent of the spanwise coordinate) distributed topography (distributed roughness). It has been found that two-dimensional distributed roughness destabilizes travelling wave disturbances (Floryan 2005; Asai & Floryan 2006), with the two-dimensional waves determining the critical conditions (Floryan 2007). The same roughness can amplify disturbances in the form of streamwise vortices (Floryan 2007). Depending on the roughness amplitude and wavenumber, and the flow Reynolds number, the first bifurcation can lead to either the onset of travelling waves or streamwise vortices. Qualitatively similar flow responses have been found in the case of Couette flow (Floryan 2002) and flow in a converging–diverging channel (Floryan 2003; Floryan & Floryan 2010). The same roughness has been found to increase transient growth with the optimal disturbances having the form of streamwise vortices (Szumbarski & Floryan 2006). The effect of transition in the form of roughness patterns is addressed by Floryan & Asai (2011). Roughness may

appear in the form of a roughness patch and the effect of the beginning and the end of the patch and the question of how quickly the flow recovers from such transition have been studied by Inasawa, Floryan & Asai (2014).

The results discussed above apply to distributed topography (distributed roughness) that has a two-dimensional form and is transverse with respect to the flow direction. The present analysis is focused on the same two-dimensional topography but oriented parallel to the flow direction and, thus, it contributes to the better understanding of the effects of distributed roughness. It is convenient to refer to this form of surface topography as longitudinal grooves or riblets, as is the case in turbulent flows. It is well known that riblets can reduce frictional drag in turbulent flow (Walsh 1983); see Dean & Bhushan (2010) and Jin & Herwig (2014) for recent reviews. It has been shown only recently that they can also reduce drag in laminar flow (Mohammadi & Floryan 2013*a*,*b*; Moradi & Floryan 2013*a*). The effect of riblets on the flow stability and laminar–turbulent transition is less understood. Techniques for the analysis of the stability of riblet-modified flows are described in Ehrenstein (1996), Szumbarski (2007) and Boiko & Nechepurenko (2010). Ehrenstein (1996) considered riblets with a scalloped cross-section and concluded that they always destabilize the flow. Rothenflue & King (1995) observed riblet-induced formation of a streamwise pair of vortices during boundary-layer transition. The same riblets amplify the growth of two-dimensional travelling waves but delay the transformation of Λ-vortices into turbulent spots (Grek, Kozlov & Titarenko 1996). In the case of three-dimensional boundary layers, riblets are able to suppress the development of travelling waves (Boiko *et al.* 1997) as well as the streak instability (Boiko *et al.* 2007). Luchini & Trombetta (1995) found that riblets slightly reduce the critical Reynolds number. The two-dimensional waves were found to be amplified and three-dimensional structures damped by the grooves in K-type transition while in the oblique transition caused by two oblique waves the breakdown to turbulence was delayed by riblets (Klamp, Meinke & Schröder 2010). Sinusoidal riblets of very high amplitude were found to produce significant destabilization in pressure-driven flows (Szumbarski 2007). The above summary demonstrates that riblets may produce a number of effects but the complete analysis is not yet available.

The primary objective of this work is to carry out a systematic analysis of the effects of small-amplitude two-dimensional grooves of various shapes and being parallel to the flow direction on the stability of pressure-driven flows in a channel. The new results expand the understanding of the effects of distributed surface roughness and how such roughness is able to influence the laminar–turbulent transition and, thus, complement results available for the same grooves placed transversely with respect to the flow (Floryan 2007). Because of the drag-reducing capabilities of the long-wavelength grooves, special attention is paid to flow stability in the presence of such grooves. Section 2 discusses the form of the mean flow. The problem formulation is given in § 2.1, the numerical solution is discussed in § 2.2, the small wavenumber approximation is presented in § 2.3 and properties of such flows are discussed in § 2.4. Section 3 is focused on the linear stability of the grooved modified flow. The problem formulation is presented in § 3.1 and the numerical solution is discussed in § 3.2. Section 4 is devoted to the presentation of the results. Sinusoidal grooves are discussed in § 4.1. Grooves with arbitrary shapes are discussed in § 4.2. The stability of flow in a channel with optimal grooves is described in § 4.3. Section 5 provides a summary of the main conclusions.

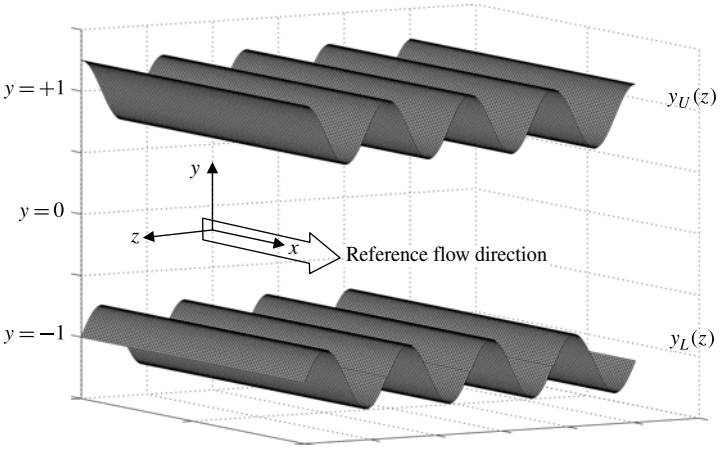

FIGURE 1. Sketch of the flow system problem.

2. Flow in a channel with longitudinal grooves

2.1. *Problem formulation*

Consider flow along a straight channel extending to $\mp\infty$ in the x direction. The flow is driven by a constant pressure gradient and has the form

$$\left.\begin{aligned} &\boldsymbol{V}_0(\boldsymbol{x}) = [u_0(\boldsymbol{x}),\, v_0(\boldsymbol{x})] = [u_0(y),\, 0] = [1 - y^2,\, 0], \quad p_0(\boldsymbol{x}) = -2x/Re \\ &\psi_0(\boldsymbol{x}) = -y^3/3 + y + 2/3, \quad Q_0 = 4/3, \end{aligned}\right\} \tag{2.1}$$

where the fluid movement is directed towards the positive x-axis, the Reynolds number Re is defined on the basis of the maximum x-velocity and the channel half-height, $\boldsymbol{x} = (x\boldsymbol{i} + y\boldsymbol{j})$, the velocity vector is defined as $\boldsymbol{V}_0 = (u_0\boldsymbol{i} + v_0\boldsymbol{j})$, ψ_0 stands for the stream function and Q_0 denotes the flow rate.

Modify this channel by placing longitudinal grooves of arbitrary shape on both walls (see figure 1). The geometry of the grooves is expressed in terms of Fourier series of the form

$$y_L(z) = -1 + \sum_{n=-N_A}^{N_A} H_L^{(n)} \mathrm{e}^{\mathrm{i}n\beta z}, \quad y_U(z) = 1 + \sum_{n=-N_A}^{N_A} H_U^{(n)} \mathrm{e}^{\mathrm{i}n\beta z} \tag{2.2a,b}$$

where $y_L(z)$ and $y_U(z)$ are the locations of the lower and upper walls, respectively, N_A is the number of Fourier modes required to describe the geometry, $\lambda = 2\pi/\beta$ denotes the groove wavelength, β stands for the wavenumber, and $H_L^{(n)} = H_L^{*(-n)}$ and $H_U^{(n)} = H_U^{*(-n)}$ are the reality conditions where stars denote complex conjugates. The choice of $H_L^{(n)}$ and $H_U^{(n)}$ is restricted by the no-contact condition between the walls. Our interest is only in grooves that do not change the mean channel opening and, thus, $H_L^{(0)} = H_U^{(0)} = 0$.

The velocity field in the grooved channel is described by the x-momentum equation of the form

$$\frac{\partial^2 u_B}{\partial z^2} + \frac{\partial^2 u_B}{\partial y^2} = Re\frac{\mathrm{d}p_B}{\mathrm{d}x} \tag{2.3}$$

where the velocity vector has components $(u_B, 0, 0)$ in the (x, y, z) directions, and is supplemented by boundary conditions of the form

$$u_B(y_L, z) = 0, \quad u_B(y_U, z) = 0. \tag{2.4a,b}$$

In the above, the subscript B is used to denote flow quantities in the grooved channel. The fixed flow rate constraint of the form

$$Q = \frac{1}{2\pi/\beta} \int_{z=0}^{z=2\pi/\beta} \int_{y=y_L(z)}^{y=y_U(z)} u_B(y, z)\, \mathrm{d}y\, \mathrm{d}z = \frac{4}{3} \tag{2.5}$$

is used as the closing condition. This constraint states that the flow rates in the smooth and grooved channels are identical. The addition of grooves changes the wall shear stress distribution as well as the wetted surface area and, thus, necessitates use of a different pressure gradient in order to maintain the same flow rate (Moradi & Floryan 2013*b*). The magnitude of the pressure gradient modification provides a quantitative measure of drag changes induced by the grooves.

Flow in the grooved channel is represented as a superposition of the smooth-channel-flow and the grooved-induced modifications, i.e.

$$\boldsymbol{V}_B(\boldsymbol{x}) = [u_B(y, z), 0, 0] = \boldsymbol{V}_0(\boldsymbol{x}) + \boldsymbol{V}_1(\boldsymbol{x}) = [u_0(y), 0, 0] + [u_1(y, z), 0, 0], \tag{2.6a}$$

$$p_B(\boldsymbol{x}) = p_0(\boldsymbol{x}) + p_1(\boldsymbol{x}) \tag{2.6b}$$

where subscript 1 identifies modifications. The resulting field equation, the boundary conditions and the constraint have the form

$$\frac{\partial^2 u_1}{\partial z^2} + \frac{\partial^2 u_1}{\partial y^2} = Re \frac{\mathrm{d}p_1}{\mathrm{d}x}, \tag{2.7}$$

$$u_0(z, y_L) + u_1(z, y_L) = 0, \quad u_0(z, y_U) + u_1(z, y_U) = 0, \tag{2.8a,b}$$

$$Q = \frac{1}{2\pi/\beta} \int_{z=0}^{z=2\pi/\beta} \int_{y=y_L(z)}^{y=y_U(z)} [u_0(y) + u_1(y, z)]\, \mathrm{d}y\, \mathrm{d}z = \frac{4}{3}. \tag{2.9}$$

2.2. *Numerical solution*

A spectrally accurate solution is desired. Two methods for dealing with the irregularities of the boundaries have been used, i.e. the IBC method (Mohammadi & Floryan 2012) and the DT method (Moradi & Floryan 2013*b*). The former method is more computationally efficient and, thus, has been used in the majority of the investigation, while the latter one has been used to investigate limiting cases and to provide an accuracy check for the IBC method. While the applicability of the IBC method is limited by the groove amplitude, it provides complete access to the amplitudes of interest in this study. The over-constrained version of this method may provide access to larger amplitudes if required (Husain *et al.* 2009). The IBC method uses a regular solution domain with the flow domain placed in its interior and enforces the flow boundary conditions as internal constraints. The spatial discretization of the field equation uses a Fourier expansion in the z direction, i.e.

$$u_1(y, z) = \sum_{n=-\infty}^{n=+\infty} u_1^{(n)}(y) \mathrm{e}^{\mathrm{i}n\beta z}, \tag{2.10}$$

where $u_1^{(n)} = u_1^{(-n)*}$ is the reality condition and star denotes the complex conjugate. The modal functions are discretized using Chebyshev expansions. The algebraic equations are constructed using the Galerkin projection method. The construction of the boundary constraints uses Fourier expansions for all boundary variables. Extraction of the lowest modes leads to the explicit form of the boundary constraints which are imposed using the tau concept (Canuto *et al.* 2006). The flow rate constraint is discretized directly and is used as the condition required for the direct evaluation of the pressure correction simultaneously with the flow field. The number of Chebyshev polynomials and Fourier modes used in the solution were arrived at through numerical experimentation and have been selected to assure a minimum of six-digit accuracy. Details of the algorithm can be found in Mohammadi & Floryan (2012). The DT method uses the same spatial discretization as the IBC method with the boundary conditions imposed in a classical manner using the tau concept. Details can be found in Moradi & Floryan (2013*b*).

2.3. *Small wavenumber approximation*

The flow field can be determined analytically for long-wavelength grooves (Mohammadi & Floryan 2013*a*). The solution domain is regularized using a transformation of the form

$$\chi = \beta z, \quad \varsigma = \frac{2[y - y_u(z)]}{y_u(z) - y_L(z)} + 1, \tag{2.11a,b}$$

which maps the grooved channel into a straight strip in the (ς, χ) plane and the χ-coordinate plays the role of a slow scale. The field equation assumes the form

$$\frac{\partial^2 u_B}{\partial \varsigma^2} + g_1(\chi, \varsigma)\frac{\partial u_B}{\partial \varsigma} + g_2(\chi, \varsigma)\frac{\partial^2 u_B}{\partial \chi \partial \varsigma} + g_3(\chi, \varsigma)\frac{\partial^2 u_B}{\partial \chi^2} - g_4(\chi, \varsigma)Re\frac{\mathrm{d}p_B}{\mathrm{d}z} = 0, \tag{2.12}$$

where the known coefficients of the form

$$\begin{aligned} g_1(\chi, \varsigma) &= \varsigma_{zz}/(\varsigma_z^2 + \varsigma_y^2),\ g_2(\chi, \varsigma) = 2\beta\varsigma_z/(\varsigma_z^2 + \varsigma_y^2),\ g_3(\chi, \varsigma) \\ &= \beta^2/(\varsigma_z^2 + \varsigma_y^2) g_4(\chi, \varsigma) \\ &= 1/(\varsigma_z^2 + \varsigma_y^2) \end{aligned} \tag{2.13}$$

contain information about the groove geometry. In the above

$$\left.\begin{aligned} &\varsigma_z = -\beta H^{-1}(G_\chi + \varsigma H_\chi), \quad \varsigma_{zz} = -\beta^2 H^{-1}(2\beta^{-1}\varsigma_z G_\chi + G_{\chi\chi} + \varsigma H_{\chi\chi}), \\ &\varsigma_y = H^{-1}, \\ &G = (y_U + y_L)/2, \quad H = (y_U - y_L)/2. \end{aligned}\right\} \tag{2.14}$$

The boundary conditions and flow rate constraint take the form

$$u_B(\chi, \mp 1) = 0, \tag{2.15}$$

$$Q = \frac{1}{2\pi}\int_{\chi=0}^{\chi=2\pi}\int_{\varsigma=-1}^{\varsigma=+1} H u_B(\chi, \varsigma)\mathrm{d}\varsigma\mathrm{d}\chi = \frac{4}{3}. \tag{2.16}$$

Assume a solution of the form

$$u_B = U_0 + \beta U_1 + \beta^2 U_2 + \beta^3 U_3 + O(\beta^4), \tag{2.17}$$

$$p_B(x) = \left(\frac{\mathrm{d}P_0}{\mathrm{d}x} + \beta\frac{\mathrm{d}P_1}{\mathrm{d}x} + \beta^2\frac{\mathrm{d}P_2}{\mathrm{d}x} + \beta^3\frac{\mathrm{d}P_3}{\mathrm{d}x}\right)x + c + O(\beta^4), \tag{2.18}$$

where c is an arbitrary constant, substitute into the field equations, the boundary conditions and the constraint and retain the four leading-order terms. The resulting systems are given in appendix A and their solutions have the form

$$\left.\begin{aligned} &U_0 = I_1^{-1}(1-\varsigma^2)H^2, \quad \mathrm{d}P_0/\mathrm{d}x = -2Re^{-1}I_1^{-1},\\ &U_1 = 0, \quad \mathrm{d}P_1/\mathrm{d}x = 0,\\ &U_2 = -I_1^{-1}(1-\varsigma^2)H^2(G_\chi^2 - H_\chi^2 - HH_{\chi\chi} - \varsigma HG_{\chi\chi}/3 - I_1^{-1}I_2),\\ &\qquad \mathrm{d}P_2/\mathrm{d}x = -2Re^{-1}I_1^{-2}I_2,\\ &U_3 = 0, \quad \mathrm{d}P_3/\mathrm{d}x = 0, \end{aligned}\right\} \tag{2.19}$$

where

$$I_1 = \frac{1}{2\pi}\int_{\chi=0}^{\chi=2\pi} H^3\mathrm{d}\chi, \quad I_2 = \frac{1}{2\pi}\int_{\chi=0}^{\chi=2\pi} H^3(G_\chi^2 - H_\chi^2 - HH_{\chi\chi})\mathrm{d}\chi. \tag{2.20a,b}$$

In the case of grooves of sinusoidal shape placed at the lower wall, i.e.

$$y_L(z) = -1 + S_L\cos(\beta z), \quad y_U(z) = 1, \tag{2.21a,b}$$

where S_L and β denote the groove amplitude and the wavenumber, respectively, the above expressions simplify to the following form

$$\left.\begin{aligned} &U_0(\chi,\varsigma) = (1+3S_L^2/8)^{-1}(1-0.5S_L\cos\chi)^2(1-\varsigma^2),\\ &\qquad \mathrm{d}P_0/\mathrm{d}x = -2Re^{-1}(1+3S_L^2/8)^{-1},\\ &U_1(\chi,\varsigma) = 0, \quad \mathrm{d}P_1/\mathrm{d}x = 0,\\ &U_2(\chi,\varsigma) = 0.5(1+3S_L^2/8)^{-1}(1-\varsigma^2)(1-0.5S_L\cos\chi)^2\\ &\qquad\qquad \times\left[S(\cos\chi - 0.5S_L\cos^2\chi)(1-\varsigma/3)\right.\\ &\qquad\qquad \left.+ (1+3S_L^2/8)^{-1}(S_L^2 + 3S_L^4/16)\right],\\ &\mathrm{d}P_2/\mathrm{d}x = -S_L^2Re^{-1}(1+3S_L^2/8)^{-2}(1+3S_L^2/16),\\ &U_3(\chi,\varsigma) = 0, \quad \mathrm{d}P_3/\mathrm{d}x = 0. \end{aligned}\right\} \tag{2.22}$$

The range of validity of the above solution can be determined by comparing the pressure losses determined using the complete solution discussed in § 2.2, i.e.

$$\left(Re\frac{\mathrm{d}p_B}{\mathrm{d}x}\right)_{err} = \left|\left(Re\frac{\mathrm{d}p_B}{\mathrm{d}x}\right)_c - \left(Re\frac{\mathrm{d}p_B}{\mathrm{d}x}\right)_a\right|, \tag{2.23}$$

where subscripts a and c denote the asymptotic and the complete solutions, respectively. The results displayed in figure 2 demonstrate that the asymptotic solution can be used up to $\beta = 0.5$ for the range of S of interest in this analysis.

2.4. *Description of the flow*

The introduction of grooves increases the wetted surface area and changes the distribution of the wall shear stress, with both of these effects contributing to changes in the drag experienced by the fluid. Results presented in figure 3 for simple sinusoidal grooves given by (2.21*a*,*b*) demonstrate that grooves with the wavenumber $\beta < \sim 0.965$ reduce the overall drag. This effect is associated with the acceleration

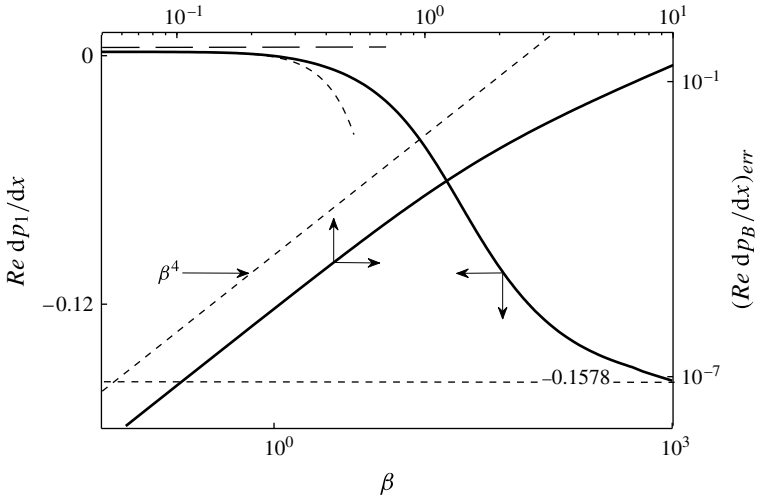

FIGURE 2. Variations of the error $(Re\,\mathrm{d}p_B/\mathrm{d}x)_{err}$ of the small-wavenumber approximation of the stationary state (see (2.23)) and variations of the pressure gradient correction $Re\,\mathrm{d}p_1/\mathrm{d}x$ for grooves with geometry described by (2.22) with the amplitude $S_L = 0.05$ as a function of the groove wavenumber β. Dotted lines identify the small β asymptote for the pressure gradient correction as well as the large β upper bound for the same quantity.

of the flow in the widest channel opening resulting in the formation of stream tubes of high-velocity fluid; see Moradi & Floryan (2013*b*) for a detailed discussion. The pressure gradient reduction is well captured by the asymptotic solution (2.22) for $\beta < \sim 0.6$ (see figure 2). The magnitude of this reduction can be increased through the use of grooves with an optimized shape (Mohammadi & Floryan 2013*a*; Moradi & Floryan 2013*a*). The flow topology becomes very simple when $\beta \to 0$ as the flow becomes nearly independent of the spanwise coordinate. The topology changes in a different manner for $\beta \to \infty$ as the grooves become narrower and viscous friction prevents the fluid from moving inside the grooves (see figure 4) forcing the flow to lift up above the grooves. The mean geometric channel opening remains the same but the effective hydraulic channel opening decreases forcing the flow to accelerate above the grooves; nevertheless, the Reynolds number remains the same due to the fixed flow rate constraint. The flow topology can be described as consisting of a nearly rectilinear flow above the grooves with a boundary layer of complex structure adjacent to the grooves. The lower bound on the pressure gradient correction can be determined by ignoring the boundary layer and approximating the flow with flow in a channel with the height reduced by S_L, i.e.

$$Re\frac{\mathrm{d}p_1}{\mathrm{d}x} = 2\left[1 - \left(1 - \frac{S_L}{2}\right)^{-3}\right]. \tag{2.24}$$

The above relation provides a good approximation for $\beta = O(10^2)$, as documented by the results displayed in figure 2.

3. Linear stability analysis

The stability properties of the flow described above are of interest due to the drag-reducing abilities of long-wavelength grooves; it is of interest to determine the

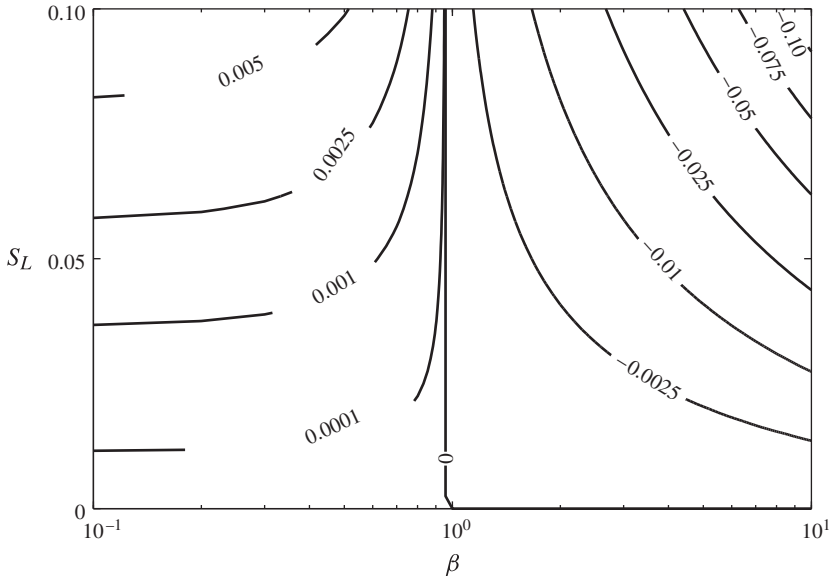

FIGURE 3. Variations of the pressure gradient correction $Re\,\mathrm{d}p_1/\mathrm{d}x$ as a function of the groove wavenumber β and the groove height S_L for the groove geometry described by (2.21*a*,*b*).

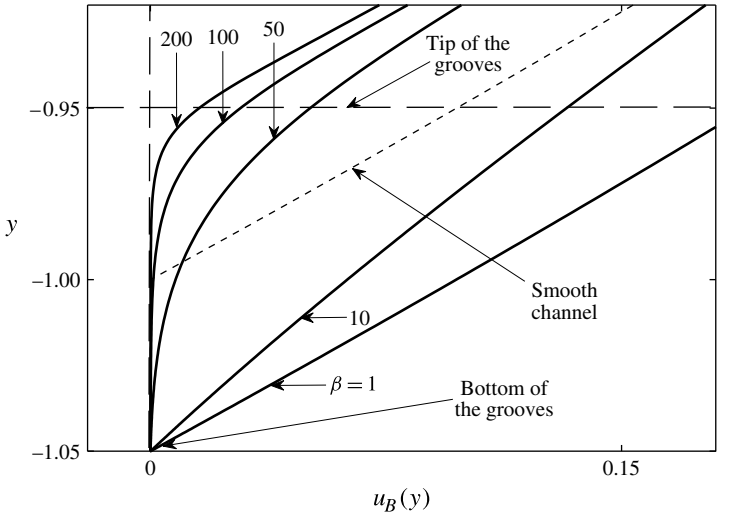

FIGURE 4. Distributions of the streamwise velocity component u_B at the widest channel opening for the groove geometry described by (2.21*a*,*b*) with the amplitude $S_L = 0.05$.

maximum Re for which such flow remains laminar. The same grooves, especially grooves with short wavelengths, represent a special category of distributed surface roughness and, thus, it is of interest to determine how such roughness affects the onset of the laminar–turbulent transition. Both questions can be addressed with the help of linear stability theory. It is assumed that the flow system has a low disturbance

level and, thus, the stability question can be addressed using the asymptotic stability concept. In the case of a noisy environment one would need to analyze transient disturbance growth (Szumbarski & Floryan 2006).

3.1. *Problem formulation*

The stability analysis begins with the governing equations expressed in terms of the vorticity transport and continuity equations, i.e.

$$\partial\boldsymbol{\omega}/\partial t-(\boldsymbol{\omega}\cdot\boldsymbol{\nabla})\boldsymbol{V}+(\boldsymbol{V}\cdot\boldsymbol{\nabla})\boldsymbol{\omega}=Re^{-1}\nabla^2\boldsymbol{\omega}, \tag{3.1a}$$

$$\boldsymbol{\nabla}\cdot\boldsymbol{V}=0, \tag{3.1b}$$

$$\boldsymbol{\omega}=\boldsymbol{\nabla}\times\boldsymbol{V}, \tag{3.1c}$$

where $\boldsymbol{\omega}$ and $\boldsymbol{V}$ denote the vorticity and velocity vectors, respectively. Three-dimensional disturbances are superposed on the base flow in the form

$$\boldsymbol{\omega}=\boldsymbol{\omega}_B(y,z)+\boldsymbol{\omega}_D(x,y,z,t),\quad \boldsymbol{V}=\boldsymbol{V}_B(y,z)+\boldsymbol{V}_D(x,y,z,t) \tag{3.2a,b}$$

where subscript D refers to the disturbance field. The flow quantities (3.2) are substituted into (3.1), the mean parts are subtracted and the equations are linearized. The resulting disturbance equations have the form

$$\begin{aligned}&\frac{\partial\xi_D}{\partial t}-\eta_B\frac{\partial u_D}{\partial y}-\frac{\partial u_B}{\partial y}\eta_D-\varphi_B\frac{\partial u_D}{\partial z}-\frac{\partial u_B}{\partial z}\varphi_D+u_B\frac{\partial\xi_D}{\partial x}\\&\quad=\frac{1}{Re}\left(\frac{\partial^2\xi_D}{\partial x^2}+\frac{\partial^2\xi_D}{\partial y^2}+\frac{\partial^2\xi_D}{\partial z^2}\right),\end{aligned} \tag{3.3a}$$

$$\begin{aligned}&\frac{\partial\eta_D}{\partial t}-\eta_B\frac{\partial v_D}{\partial y}-\varphi_B\frac{\partial v_D}{\partial z}+u_B\frac{\partial\eta_D}{\partial x}+\frac{\partial\eta_B}{\partial y}v_D+\frac{\partial\eta_B}{\partial z}w_D\\&\quad=\frac{1}{Re}\left(\frac{\partial^2\eta_D}{\partial x^2}+\frac{\partial^2\eta_D}{\partial y^2}+\frac{\partial^2\eta_D}{\partial z^2}\right),\end{aligned} \tag{3.3b}$$

$$\begin{aligned}&\frac{\partial\varphi_D}{\partial t}-\eta_B\frac{\partial w_D}{\partial y}-\varphi_B\frac{\partial w_D}{\partial z}+u_B\frac{\partial\varphi_D}{\partial x}+\frac{\partial\varphi_B}{\partial y}v_D+\frac{\partial\varphi_B}{\partial z}w_D\\&\quad=\frac{1}{Re}\left(\frac{\partial^2\varphi_D}{\partial x^2}+\frac{\partial^2\varphi_D}{\partial y^2}+\frac{\partial^2\varphi_D}{\partial z^2}\right),\end{aligned} \tag{3.3c}$$

$$\frac{\partial u_D}{\partial x}+\frac{\partial v_D}{\partial y}+\frac{\partial w_D}{\partial z}=0, \tag{3.3d}$$

where $\boldsymbol{\omega}_B=(0,\eta_B,\varphi_B)$, $\boldsymbol{V}_D=(u_D,v_D,w_D)$ and $\boldsymbol{\omega}_D=(\xi_D,\eta_D,\varphi_D)$. The homogeneous boundary conditions of the form

$$\boldsymbol{V}_D(x,y,z,t)=0\quad\text{at } y=y_L(z)\text{ and } y=y_U(z) \tag{3.4}$$

complete the formulation. Equations (3.3*a*) have coefficients that are functions of y and z and, thus, the solution can be written in the form

$$\boldsymbol{V}_D(x,y,z,t)=\boldsymbol{G}_D(y,z)\mathrm{e}^{\mathrm{i}(\delta x+\mu z-\sigma t)}+\text{c.c.} \tag{3.5a}$$

$$\boldsymbol{\omega}_D(x,y,z,t)=\boldsymbol{\Omega}_D(y,z)\mathrm{e}^{\mathrm{i}(\delta x+\mu z-\sigma t)}+\text{c.c.} \tag{3.5b}$$

where δ and μ are the real wavenumbers, $\sigma = \sigma_r + \mathrm{i}\sigma_i$, σ_i describes the rate of growth of disturbances, σ_r describes their frequency and c.c. stands for complex conjugate, i.e. the stability problem is posed as the temporal stability. Here $\boldsymbol{G}_D(y, z)$ and $\boldsymbol{\Omega}_D(y, z)$ are the z-periodic amplitude functions and, thus, they can be expressed in terms of the Fourier series of the form

$$\boldsymbol{G}_D(y, z) = \sum_{m=-\infty}^{m=+\infty} [g_u^{(m)}(y), g_v^{(m)}(y), g_w^{(m)}(y)]\mathrm{e}^{\mathrm{i}m\beta z} + \text{c.c.} \tag{3.6a}$$

$$\boldsymbol{\Omega}_D(y, z) = \sum_{m=-\infty}^{m=+\infty} [g_\xi^{(m)}(y), \mathrm{i}g_\eta^{(m)}(y), g_\varphi^{(m)}(y)]\mathrm{e}^{\mathrm{i}m\beta z} + \text{c.c.} \tag{3.6b}$$

Substitution of (3.6) into (3.5) leads to the disturbance velocity and vorticity components of the form

$$\boldsymbol{V}_D(x, y, z, t) = \sum_{m=-\infty}^{m=+\infty} [g_u^{(m)}(y), g_v^{(m)}(y), g_w^{(m)}(y)]\mathrm{e}^{\mathrm{i}[\delta x + (\mu + m\beta)z - \sigma t]} + \text{c.c.} \tag{3.7a}$$

$$\boldsymbol{\omega}_D(x, y, z, t) = \sum_{m=-\infty}^{m=+\infty} [g_\xi^{(m)}(y), \mathrm{i}g_\eta^{(m)}(y), g_\varphi^{(m)}(y)]\mathrm{e}^{\mathrm{i}[\delta x + (\mu + m\beta)z - \sigma t]} + \text{c.c.} \tag{3.7b}$$

Substitution of (3.7) and (2.10) into (3.3) and separation of Fourier modes leads, after rather lengthy algebra, to a system of linear ordinary differential equations for $g_\eta^{(m)}(y)$ and $g_v^{(m)}(y)$ of the form

$$T^{(m)}(y)g_v^{(m)}(y) = \sum_{n=-\infty}^{n=+\infty} [H_v^{(m,n)}(y)g_v^{(m-n)}(y) + H_\eta^{(m,n)}(y)g_\eta^{(m-n)}(y)], \tag{3.8a}$$

$$S^{(m)}(y)g_\eta^{(m)}(y) + C^{(m)}(y)g_v^{(m)}(y) = \sum_{n=-\infty}^{n=+\infty} [E_v^{(m,n)}(y)g_v^{(m-n)}(y) + E_\eta^{(m,n)}(y)g_\eta^{(m-n)}(y)] \tag{3.8b}$$

where $-\infty < m < +\infty$ and the explicit forms of the operators T, S, C, E_v, E_η, H_v, H_η are given in appendix B. The above formulation is similar to the Bloch theory (Bloch 1928) for systems with spatially periodic coefficients and to the Floquet theory (Coddington & Levinson 1965) for systems with time periodic coefficients. Groove effects are contained in the right-hand side (RHS) of (3.8) and in the boundary conditions (3.4). When the groove amplitude approaches zero, the RHS becomes zero and the modal equations decouple. In this limit, (3.8) describe a system of oblique Tollmien–Schlichting (TS) waves propagating independently of each other. In analogy to the stability of parallel flows, we shall refer to the T, S and C operators as the TS, Squire and coupling operators, respectively (Floryan 1997).

Equations (3.8) together with the homogeneous boundary conditions (3.4) form an eigenvalue problem and have a non-trivial solution only for certain combinations of (δ, μ, σ) for the specified flow conditions (Re) and for the specified groove geometry $(\beta, H_L^{(n)}, H_U^{(n)})$. The required dispersion relation has to be determined numerically and the relevant methodology is described in the next section.

3.2. *Numerical solution*

The problem to be solved consists of an infinite system of ordinary differential equations (3.8) with the homogeneous boundary conditions (3.4). The Fourier expansions (3.7) are truncated after term N_N and the modal functions are discretized using the Chebyshev expansions of order N_T of the form

$$[g_v^{(m)}(y), g_\eta^{(m)}(y)] = \sum_{k=0}^{+\infty} [G_{k,v}^{(m)}, G_{k,\eta}^{(m)}] T_k(y) \approx \sum_{k=0}^{N_T} [G_{k,v}^{(m)}, G_{k,\eta}^{(m)}] T_k(y), \tag{3.9}$$

where T_k denotes the Chebyshev polynomial of the kth order, and $G_{k,v}^{(n)}$ and $G_{k,\eta}^{(n)}$ stand for the unknown coefficients of the expansions. The Galerkin projection method is used to form a system of linear algebraic equations. Details of the discretization process are presented in appendix C.

The homogeneous boundary conditions are enforced using the IBC method (Szumbarski & Floryan 1999; Floryan 2002). Appendix D provides details of the discretization process. Four equations for $G_{k,v}^{(n)}$ and two equations for $G_{k,\eta}^{(n)}$ corresponding to the highest Chebyshev polynomials are eliminated for each Fourier mode providing space for the imposition of the boundary relations (tau method). An over-constrained version of this method provides access to larger groove amplitudes (Husain *et al.* 2009). The DT method (Cabal, Szumbarski & Floryan 2002) provides another alternative if grooves with very large amplitudes are of interest.

The resulting homogeneous algebraic system can be posed in various ways. For the global solution the system is posed as a general eigenvalue problem of the form

$$AE = \sigma BE, \tag{3.10}$$

where E denotes the eigenvectors and the σ-spectrum is determined numerically. These solutions are expensive numerically and suffer from accuracy problems when large matrices are involved. Efficiencies can be found by using the Arnoldi method (Saad 2003) which permits evaluation of only a selected part of the spectrum. Local solutions are still more computationally efficient and more accurate but produce a limited number of eigenvalues, mostly just one eigenvalue. These solutions are used for tracing selected eigenvalues through the parameter space. The process starts with an initial guess either for the eigenvalue or for the eigenvector and iterations are used to converge to the true eigenvalue and/or eigenvector.

Three methods for eigenvalue tracing have been used. In the first method, one of the homogeneous boundary conditions is replaced by an inhomogeneous boundary condition imposed on a different quantity resulting in an inhomogeneous system which can be easily solved. The true eigenvalue is found if the solution of the inhomogeneous system happens to satisfy the eliminated boundary condition. Since this is not true in general, the eigenvalue is searched for by looking for the zero of the replaced boundary condition using the Newton–Raphson procedure. The boundary condition for the vertical velocity component at the lower wall has been replaced in this study with a condition for the second derivative of the vertical velocity component. A good initial guess for σ significantly accelerates convergence. In the second method the eigenvalue is searched for by looking for zeros of determinant of $(A - \sigma B)$ where the system is posed as

$$(A - \sigma B)E = 0. \tag{3.11}$$

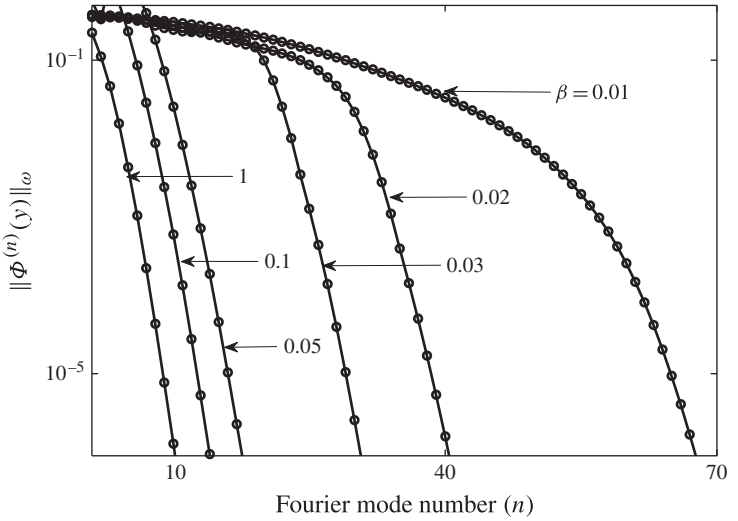

FIGURE 5. Variations of the Chebyshev norm $\|\Phi^{(n)}(y)\|_\omega$ (see (3.14)) as a function of the Fourier mode number n for the groove geometry described by (2.21*a*,*b*) with $S_L = 0.05$ for the flow Reynolds number $Re = 6500$ and the disturbance wavenumbers $\delta = 1.02$ and $\mu = 0$.

In the third method, the inverse iterations method, we compute an approximation for the eigenvector E_a corresponding to the unknown eigenvalue σ_a using an iterative process in the form

$$(A - \sigma_0 B)E^{(n+1)} = BE^{(n)}, \tag{3.12}$$

where σ_0 and $E^{(0)}$ are the eigenvalue and the eigenvector (an eigenpair) corresponding to the unaltered flow. If σ_a is the eigenvalue closest to σ_0, $E^{(n)}$ converges to E_a. The eigenvalue σ_a is evaluated using

$$\sigma_a = E_a^{(n)\mathrm{T}} A E_a^{(n)} / E_a^{(n)\mathrm{T}} B E_a^{(n)} \tag{3.13}$$

where 'T' denotes the complex conjugate transpose. The inverse iterations method was found to be generally more efficient compared with the Newton–Raphson method. The tracing of eigenvalues has been extended over several Brillouin zones (Bloch 1928) in the μ direction in order to demonstrate how the leading eigenvalue is affected by the groove wavelength. The tracing process needs to be carefully implemented for small β as the widths of the Brillouin zones decrease rapidly and the eigenvalues become tightly spaced.

The accuracy and cost of the discretization depend on the rate of convergence of expansions (3.7) as well as the Fourier expansions used in the construction of the boundary constraints (see appendix D). Convergence can be assessed using the energy of the Fourier modes, which is measured using the Chebyshev norm for the x-component of the disturbance velocity, i.e. $g_u^{(m)}(y)$, defined as

$$\|\Phi^{(n)}(y)\|_\omega = \left\{ \int_{-1}^{1} g_u^{(m)}(y) g_u^{(m)*}(y) \omega(y)\, \mathrm{d}y \right\}^{1/2}, \tag{3.14}$$

where $\omega(y) = 1/\sqrt{1-y^2}$ and star denotes complex conjugate. Results presented in figure 5 demonstrate that the rate of convergence of these expansions strongly

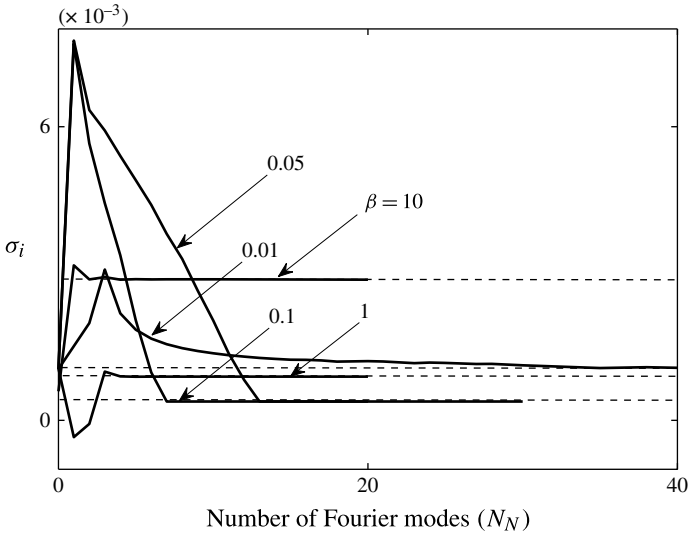

FIGURE 6. Variations of the growth rate σ_i of disturbances with the wavenumbers $\delta = 1.02$ and $\mu = 0$ as a function of the number of Fourier modes used in the numerical solution of the stability problem for flow with the Reynolds number $Re = 6500$ in the grooved channel with the groove geometry described by (2.21*a*,*b*) with $S_L = 0.05$.

depends on β. The convergence is very good for $\beta \geqslant 0.1$ and use of 10 Fourier modes guarantees a minimum of six-digit accuracy. A decrease of β leads to a significant reduction of the convergence rate and achieving the same accuracy with $\beta = 0.01$ requires use of around 70 Fourier modes. The evaluation of the eigenvalues requires fewer modes as illustrated in figure 6, e.g. use of just five modes gives six-digit accuracy when $\beta \geqslant 0.1$ but around 30 modes are required for $\beta = 0.01$.

4. Results

It is known that flow in a smooth channel becomes unstable at $Re = 5772.2$ with the two-dimensional TS waves with the wavenumber $\delta = 1.0205$ travelling in the downstream direction playing the critical role (Orszag 1971). Once these waves reach sufficient amplitude, the disturbance growth becomes dominated by a three-dimensional secondary instability driven by a parametric resonance (Orszag & Patera 1983). The instability has a subcritical character and an increase of the level of disturbances can reduce the critical Reynolds number down to $Re \approx 2700$ (Herbert 1977). For a sufficiently high level of environmental disturbances the instability process can be dominated by the transient growth of disturbances with the optimal disturbances rather than the TS waves playing the critical role (Szumbarski & Floryan 2006). The addition of grooves is expected to modify travelling waves but, at the same time, it might create new disturbance structures at the onset.

The role of the grooves in the instability process depends on their shape and amplitude. We begin the discussion with the simple sinusoidal grooves placed at the lower wall only. The channel geometry is described by (2.21) with the amplitude S_L and the wavenumber β being the only geometrical parameters. This geometry corresponds to the leading Fourier mode in the Fourier expansion (2.2) representing an arbitrary groove shape. We shall limit our interests to small groove amplitudes, i.e. $S_L \leqslant 0.05$.

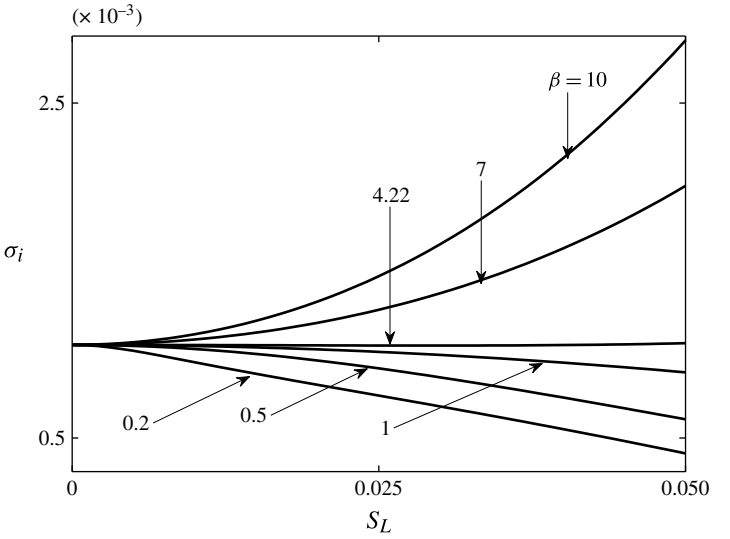

FIGURE 7. Variation of the growth rate σ_i of disturbances with the wavenumbers $\delta = 1.02$ and $\mu = 0$ as a function of the groove amplitude S_L for the groove geometry described by (2.21*a*,*b*) for flow with the Reynolds number $Re = 6500$.

4.1. *Sinusoidal grooves*

The investigation of spectra under a variety of conditions has led to the conclusion that there is only one class of unstable disturbances exists in the range of parameters considered; these disturbances connect to the classical travelling waves in the limit of $S_L \to 0$. No sign of any instability that may lead to the formation of streamwise vortices has been found. This should not be surprising as longitudinal grooves do not generate the centrifugal force field which is responsible for the formation of such vortices in the case of transverse grooves (Floryan 2003).

The transition between the characteristics of disturbances in the grooved and smooth channels is illustrated in figure 7 for a wide range of β. It can be seen that disturbances in the grooved channel evolve towards the same travelling wave as S_L is reduced. Figure 8 displays variations of the critical Reynolds number as a function of the orientation of the disturbance wavevector. The wavevector is defined as $\boldsymbol{q} = (\delta, \mu)$, it has magnitude $|\boldsymbol{q}| = (\delta^2 + \mu^2)^{1/2}$ and its orientation is expressed in terms of the inclination angle defined as $\theta = \pm \tan^{-1}(\mu/\delta)$. During test computations the magnitude of the wavevector was kept constant while its orientation was varied. It can be seen that disturbances with the wavevector aligned with the flow direction have the smallest Re_c. Although the Squire theorem (Squire 1933) does not apply to flows in grooved channels, these results lead to a conclusion equivalent to the Squire theorem. The reader may note that the critical disturbances are not two-dimensional in the grooved channel due to the modulating effect of the geometry. We shall, nevertheless, refer to these disturbances as 'two-dimensional' waves based on their properties in the limit $S_L \to 0$. The rest of this discussion will be focused on the 'two-dimensional' waves unless otherwise explicitly noted.

Results displayed in figure 7 demonstrate that grooves may either stabilize or destabilize the flow depending on the groove wavenumber, with transition occurring at $\beta = \beta_{tran} \approx 4.22$ and being independent of the groove amplitude. Grooves with

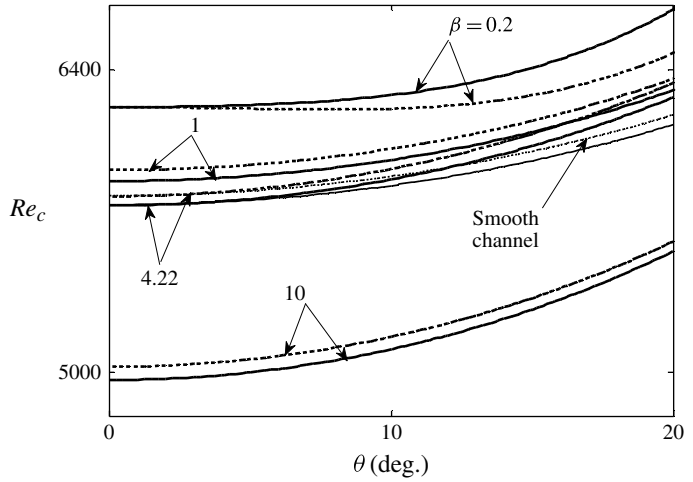

FIGURE 8. Variations of the critical Reynolds number of disturbances with the wavevector $\boldsymbol{q} = (\delta, \mu)$ of constant magnitude as a function of its inclination angle θ for the groove geometry described by (2.21*a*,*b*) with the amplitude $S_L = 0.05$. Solid lines correspond to $|\boldsymbol{q}| = 1.02$ and dotted lines to $|\boldsymbol{q}| = 1.0$.

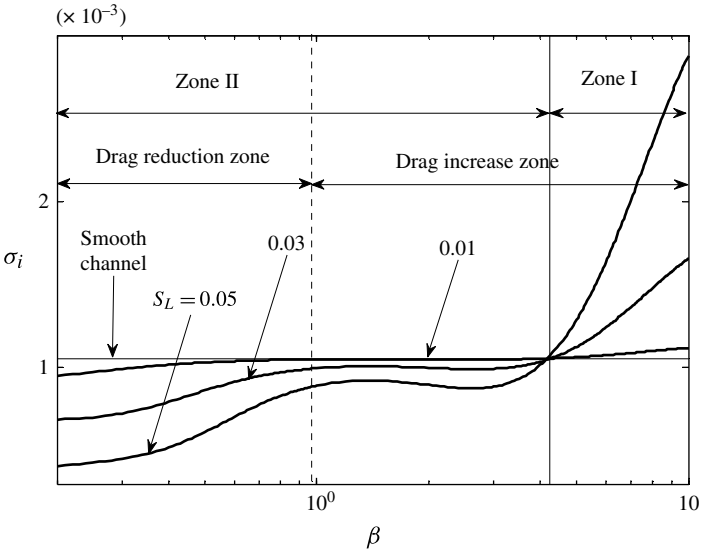

FIGURE 9. Variations of the growth rate σ_i of disturbances with the wavenumber $\delta = 1.02$ as a function of the groove wavenumber β for the groove geometry described by (2.21*a*,*b*) for flow with the Reynolds number $Re = 6500$. The dotted-line indicates the wavenumber that separates the drag reducing and drag increasing zones.

shorter wavelengths destabilize the flow with the growth rate increasing rapidly with an increase of S_L. Long-wavelength grooves stabilize the flow but the decrease of the amplification rate is much weaker than the increase observed for the short-wavelength grooves. The qualitatively different effects of β are well illustrated in figure 9 which displays variations of the amplification rate as a function of β for fixed S_L. Rapid

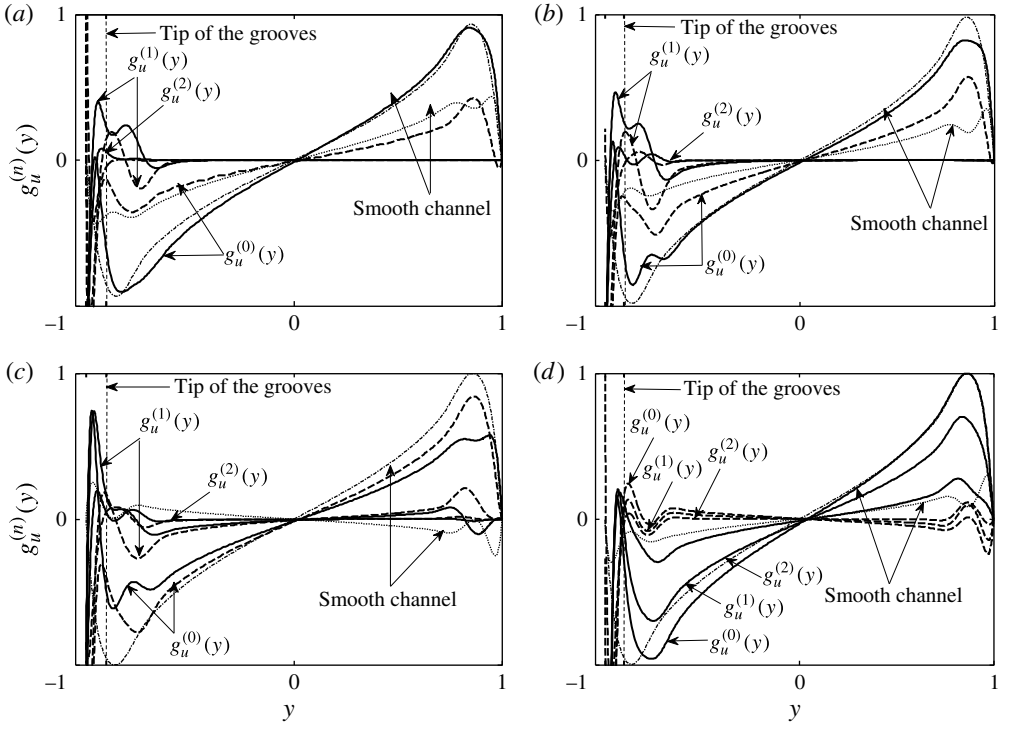

FIGURE 10. Eigenfunctions $g_u^{(n)}(y)$, $n=0$, 1, 2, describing two-dimensional travelling-wave disturbances with the wavenumber $\delta = 1.02$ in a channel with grooves whose geometry is described by (2.21*a*,*b*) with $S_L = 0.05$. Results displayed in (*a–d*) correspond to the onset conditions for the groove wavenumbers $\beta = 10$, 4.22, 1.0 and 0.2, i.e. $Re_{cr} = 5028.5$, 5773.5, 5886 and 6227.5, respectively. The normalization condition $\max_{y\in[0,1]} |g_u^{(0)}(y)| = 1$ has been used for the presentation purposes. Solid and dashed lines identify the real and imaginary parts. Thin dashed-dotted and dotted lines identify the real and imaginary parts of the eigenfunction for the smooth channel with the same Reynolds number.

destabilization in zone I (large β) as well as gradual stabilization in zone II ($\beta = 0(1)$) are clearly visible. The groove wavenumber that corresponds to the transition between the drag reducing and the drag increasing grooves, i.e. β_{cr}, lies deep inside zone II and does not have any significance as far as stability properties of the flow are concerned.

Eigenfunctions $g_u^{(n)}(y)$ corresponding to the onset conditions, i.e. condition where the amplification rate changes sign from negative to positive, displayed in figure 10 for a wide range of β permit description of the disturbance flow topology. The eigenfunctions are normalized with the maximum of $g_u^{(0)}(y)$ in the upper half of the channel, i.e. $\max_{y\in[0,1]} |g_u^{(0)}(y)| = 1$. It can be seen that near the upper (smooth) wall and for large β the dominant eigenfunctions, i.e. eigenfunctions with index 0, are very similar to the eigenfunction in a smooth channel; higher eigenfunctions are negligible in this zone. Significant differences appear when β is reduced below $\beta_{tran} \approx 4.22$ with the magnitudes of the higher eigenfunctions reaching the level of approximately 80 % of the dominant eigenfunction. The reader may note the appearance of large differences between the phase of the dominant 'grooved' eigenfunction and the 'smooth' eigenfunction. Analysis of the lower part of the channel shows that higher eigenfunctions are always important close to the grooved wall; their magnitudes

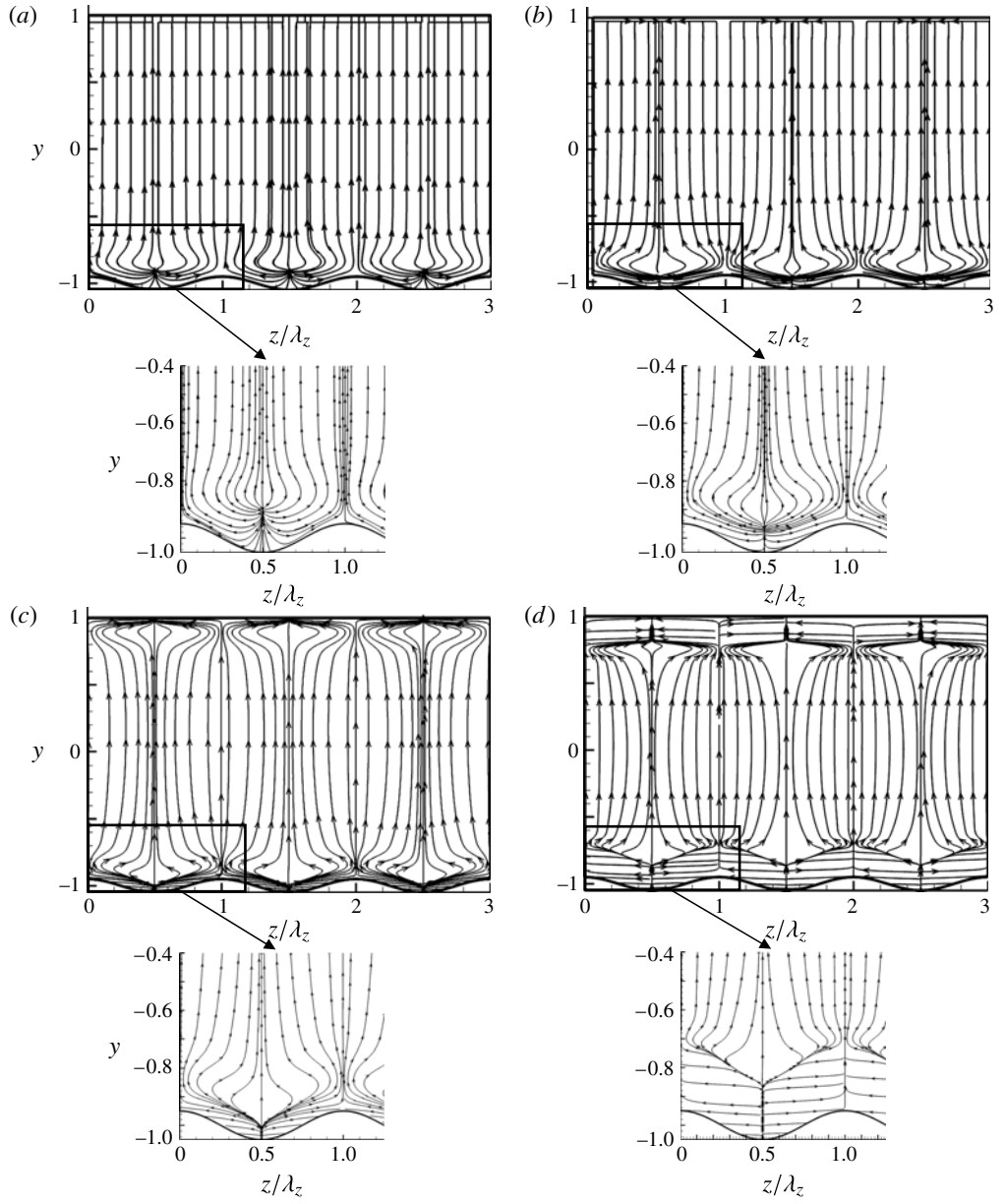

FIGURE 11. Pathlines in the y–z plane for the disturbance flow field corresponding to 'two-dimensional' disturbances with the wavenumber $\delta = 1.02$ at the onset for flow in a channel with grooves described by (2.21*a*,*b*) with $S_L = 0.05$. (*a*–*d*) display results for $(\beta, Re_c) = (10,\ 5028.5),\ (4.22,\ 5773.5),\ (1.0,\ 5886),\ (0.2,\ 6227.5)$, respectively.

increase from approximately 20 % of the dominant eigenfunction at large β to approximately 80 % at small β. Noticeable differences in the phase distribution of the 'smooth' and the dominant 'grooved' eigenfunctions can already be seen at large β; these differences increase significantly as β decreases.

The topology of the disturbance velocity field at the onset is complex, highly three-dimensional and dependent on β, as illustrated in figures 11 and 12. Pathlines

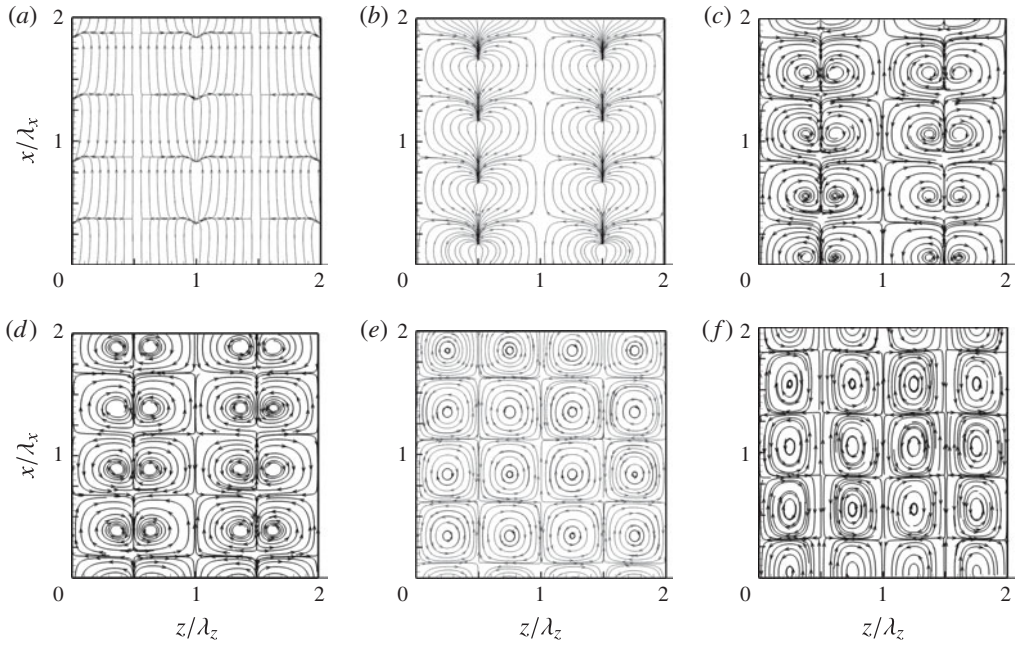

FIGURE 12. Pathlines in the x–z plane at $y = 0$ for the disturbance flow field corresponding to 'two-dimensional' disturbances with the wavenumber $\delta = 1.02$ at the onset for flow in a channel with grooves described by (2.21*a*,*b*) with $S_L = 0.05$. (*a*–*f*) display results for $(\beta, Re_c) = (10, 5028.5)$, (5, 5652.4), (4.35, 5755), (4.22, 5773.5), (1.0, 5886), (0.5, 6073.1), respectively.

in the y–z plane displayed in figure 11 demonstrate the simple structure of the flow in the upper part of the channel for large enough β (see figure 11*a*,*b*) being replaced by progressively more complex, three-dimensional topology as β decreases (see figure 11*c*,*d*). At small enough β the topology corresponds to the appearance of a sink at the wall in the narrowest channel opening (figure 11*c*) and, for a still smaller β, it is supplemented by a source at a small distance away from the wall in the widest channel opening (figure 11*d*), giving the appearance of the formation of a separation bubble. The flow topology close to the lower wall is more complex. At large β (figure 11*a*), a source appears at the trough producing a structure similar to a separation bubble. A decrease of β eliminates this bubble (see figure 11*b*). A further decrease of β increases the strength of this source, resulting in an unusual structure displayed in figure 11(*c*). At $\beta = 0.2$ (figure 11*d*) the topology corresponds to that created by a line source parallel to the wall with the wall acting like a sink resulting in the formation of a distinct layer of trapped fluid adjacent to the wall. A high level of three-dimensionality of the flow field is underscored by the form of the pathlines in the (x, z) plane at a fixed y. Figure 12 displays such pathlines at $y = 0$ for several values of β at the onset. Pathlines look like spirals for $\beta \approx \beta_{tran} \approx 4.22$ (see figure 12*c*,*d*), they look like closed loops for smaller β (see figure 12*e*,*f*), but appear to correspond to sets of point/line sinks for larger β (see figure 12*a*,*b*).

The neutral curves for the 'two-dimensional' waves in the (δ, Re) plane are fairly similar to the analogous curves for the smooth channel, as illustrated in figure 13. At small β the critical Reynolds number decreases as the groove amplitude

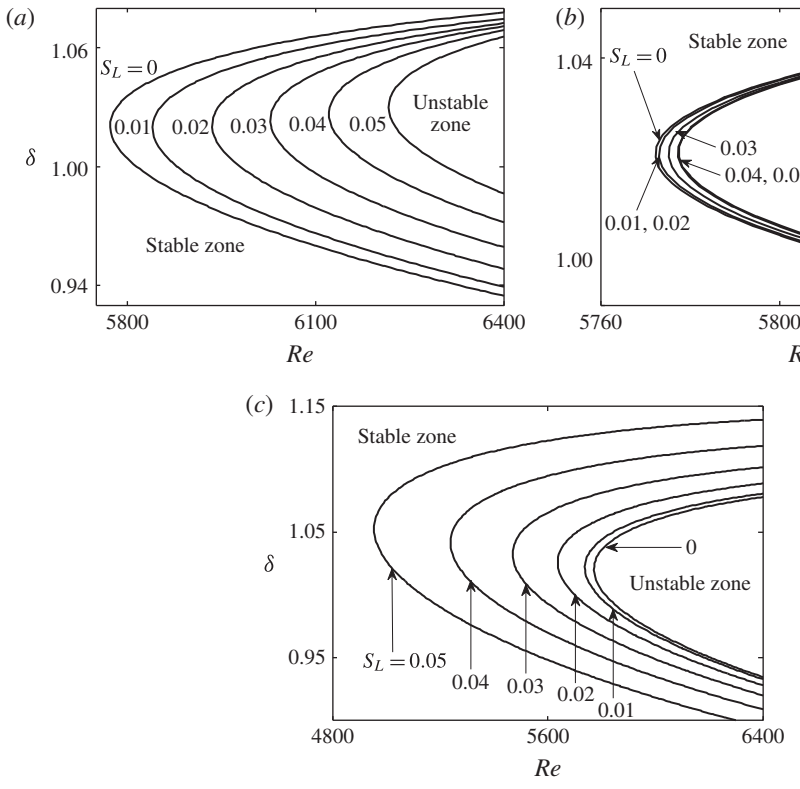

FIGURE 13. Neutral curves in the (Re, δ)-plane for the 'two-dimensional' disturbances in a channel with grooves whose geometry is described by (2.21*a*,*b*). (*a–c*) display results for the groove wavenumbers $\beta = 0.2,\ 4.22,\ 10$, respectively.

increases while the critical disturbance wavenumber δ_{cr} remains nearly unchanged (figure 13*a*). At $\beta = \beta_{tran}$ both Re_c and δ_{cr} are marginally affected by variations of S_L (figure 13*b*). At large β the critical Reynolds numbers decreases as S_L increases while δ_{cr} marginally increases.

The stabilizing/destabilizing effects of the grooves are well illustrated by the neutral curves in the (β, δ) plane. Figure 14(*a*) displays results for the nominally subcritical Reynolds number $Re = 5500$. The flow is stable for small enough β but becomes unstable once β reaches a certain minimum value; a further increase of β results in a large expansion of the range of the unstable δ. The minimum value of β required for the onset of the instability decreases with an increase of S_L. A similar process can be observed for the nominally critical Reynolds number $Re = 5772.25$ (see figure 14*b*) where there is only one unstable δ for small enough β, but its range expands once β reaches a certain minimum, S_L-dependent value. Figure 14(*c*) corresponds to the nominally supercritical Reynolds number $Re = 6000$. It can be seen that an increase of S_L decreases the range of unstable δ for small βs, even leading to complete flow stabilization. The process is opposite for $\beta > \beta_{tran} \approx 4.22$ where a large expansion of the unstable δ is observed.

Figure 15 illustrates variations of the critical Reynolds number Re_c as a function of β and S_L and provides a basis for a compact summary of the main results. The flow stability is not affected by the grooves with $\beta = \beta_{tran} \approx 4.22$ regardless of

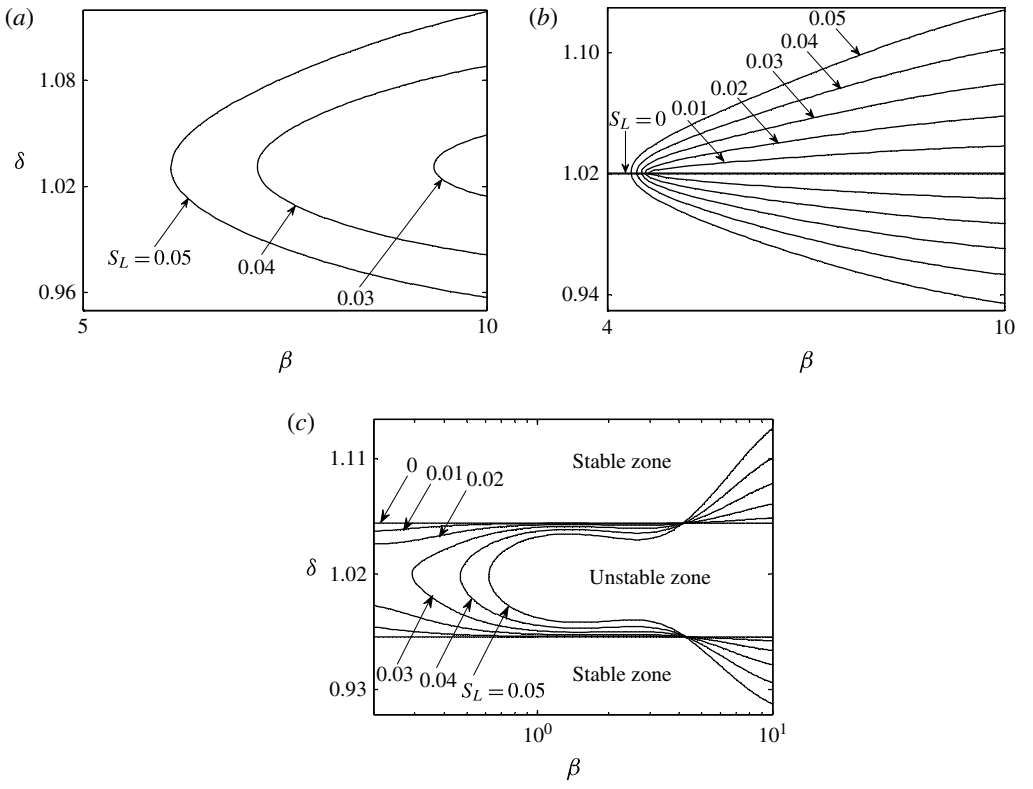

FIGURE 14. Neutral curves in the (β, δ)-plane for the 'two-dimensional' disturbances in a channel with grooves whose geometry is described by (2.21*a*,*b*). (*a–c*) display results for flow with $Re = 5500, 5772.25, 6000$, respectively.

their amplitude. The flow is destabilized for larger β with Re_c decreasing with an increase of β and this destabilization is more effective for larger S_L. The smallest critical Reynolds number of $Re_c = 4955$ is achieved for $\beta = 10$ and $S_L = 0.05$ which are the upper limits of these parameters considered in the present study; further reduction of Re_c might be achieved with larger groove amplitudes and wavenumbers. The flow is stabilized for $\beta < \beta_{tran} \approx 4.22$ as Re_c increases with a decrease of β; the stabilization is more effective for larger S_L. The largest critical Reynolds number of $Re_c = 6138$ is achieved for $\beta = 0.4$ and $S_L = 0.05$ which define the limits of the present investigation.

The effect of the placement of the grooves on both walls is illustrated in figures 16–20. The channel geometry is described as

$$y_L(z) = -1 + S_L \cos(\beta z), \quad y_U(z) = 1 + S_U \cos(\beta z + \phi) \qquad (4.1a,b)$$

i.e. both sets of grooves have the same amplitude but the upper grooves are shifted by ϕ with respect to the lower grooves. Figure 16 corresponds to $\phi = \pi$, i.e. the channel assumes the converging–diverging form. The range of drag-reducing grooves expands to $\beta < 1.2$, i.e. it is larger than that achieved with grooves on one wall only (compare figures 3 and 16*a*), and the magnitude of drag reduction increases by a factor of up to five. This effect is associated with a more efficient formation of the

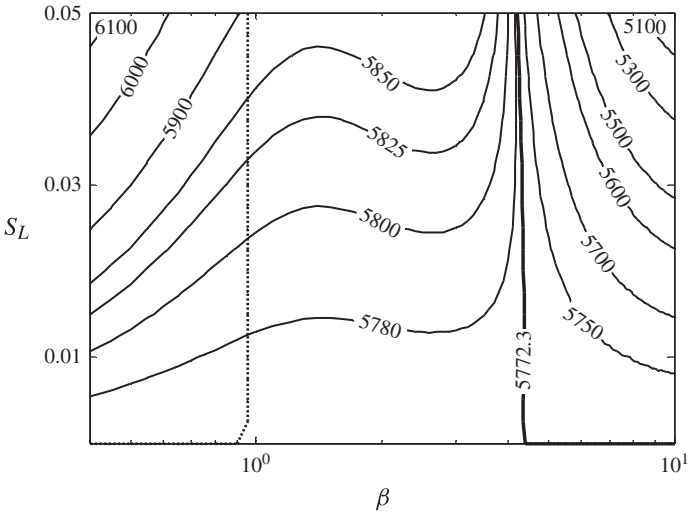

FIGURE 15. Variations of the critical Reynolds number Re_c as a function of the groove wavenumber β and the groove amplitude S_L for channel with geometry described by (2.21*a*,*b*). The dotted-line corresponds to $Re\,\mathrm{d}p_1/\mathrm{d}x = 0$.

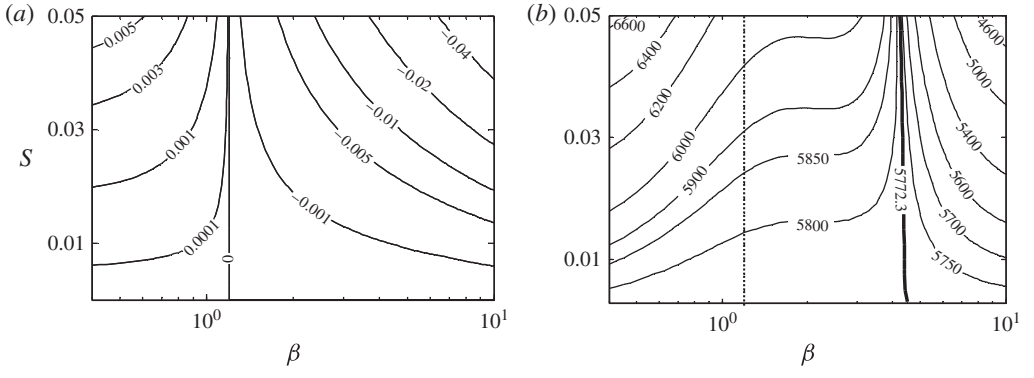

FIGURE 16. Variations of the pressure gradient correction $Re\,\mathrm{d}p_1/\mathrm{d}x$ (*a*) and the critical Reynolds number Re_c (*b*) as a function of the groove wavenumber β and the groove height S ($= S_U = S_L$) for the channel geometry given by (4.1) with $\phi = \pi$. The dotted line in (*b*) corresponds to $Re\,\mathrm{d}p_1/\mathrm{d}x = 0$.

high-velocity stream tubes in the widest channel opening; these tubes are essential for the drag reduction (Mohammadi & Floryan 2013*b*; Moradi & Floryan 2013*a*). The flow stability is not affected by the grooves with $\beta = \beta_{tran} \approx 4.4$, and the flow is more destabilized by the short wavelength grooves as well as more stabilized by the long-wavelength grooves (compare figures 15 and 16*b*). Figure 17 corresponds to $\phi = \pi/2$. The range of drag-reducing grooves is limited to $\beta < 0.9575$ and the maximum possible drag reduction is reduced to approximately 50 % of that achieved with $\phi = \pi$. The critical Reynolds number Re_c is not affected by grooves with $\beta = \beta_{tran} \approx 4.35$, the long-wavelength grooves are less effective in flow stabilization but the short-wavelength grooves remain as effective in flow destabilization as for $\phi = \pi$. Figure 18 corresponds to $\phi = 0$, i.e. the channel assumes a wavy form. Such grooves

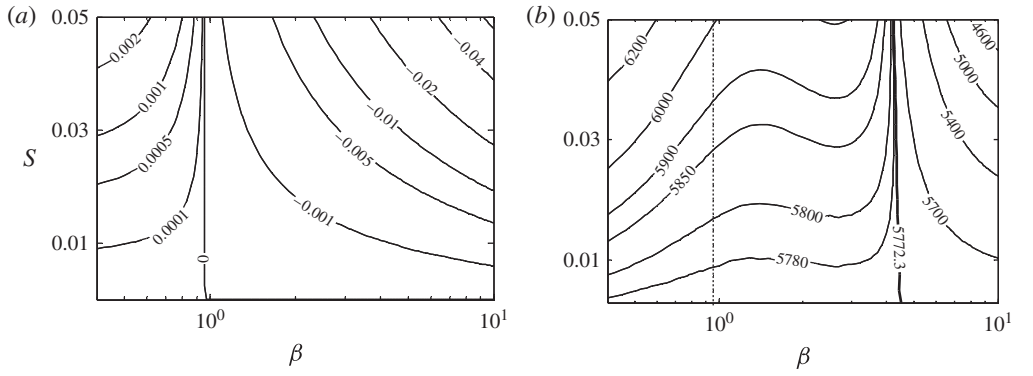

FIGURE 17. The same as in figure 16 but for the channel geometry given by (4.1) with $\phi = \pi/2$.

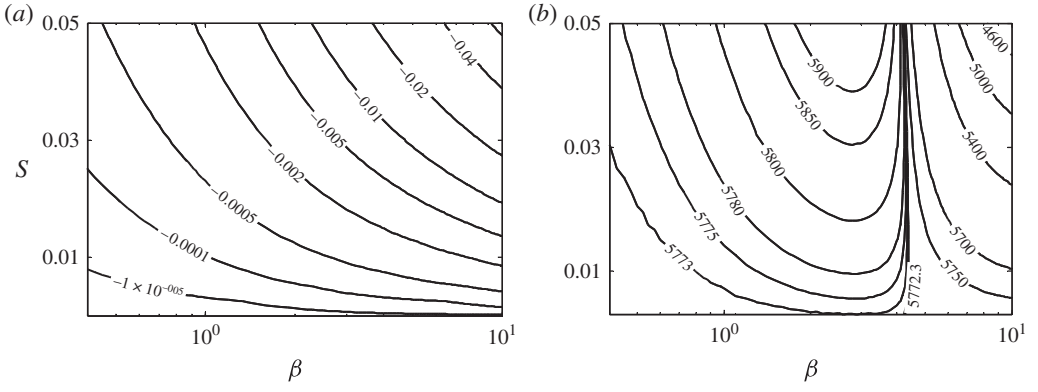

FIGURE 18. The same as in figure 16 but for the channel geometry given by (4.1) with $\phi = 0$.

are unable to reduce drag as shown in figure 18(*a*); this is related to the fact that the high-velocity stream tubes cannot be formed as channel opening varies minimally in the spanwise direction. The critical Re is not affected by grooves with $\beta = \beta_{tran} \approx 4.35$. The short-wavelength grooves are as effective in flow destabilization as other groove configurations. The long-wavelength grooves stabilize the flow for $1 < \beta < 4.35$ but the stabilizing effect disappears for longer wavelengths (figure 18*b*). The effects of the phase shift between the upper and lower groove systems are summarized in figure 19. Grooves lose drag-reducing capability for $\phi < 0.5$ for all β studied; their drag-reducing ability is confined to the left upper corner in the (ϕ, β) plane (see figure 19*a*) and this is where the largest flow stabilization is observed (figure 19*b*). The relative position of the short-wavelength grooves does not affect their stability characteristics as all of them reduce Re_c at the same rate; this is related to the groove-induced stream lift-up phenomenon (Mohammadi & Floryan 2013*b*). Figure 20 illustrates effects of the phase shift for the unequal groove amplitudes at both walls. The drag-reducing ability is preserved for all ϕ as the channel opening changes in the spanwise direction. The flow stabilization in the left upper corner is less effective than for grooves with equal amplitudes (figure 19) and, similarly, flow destabilization for large β is less extreme.

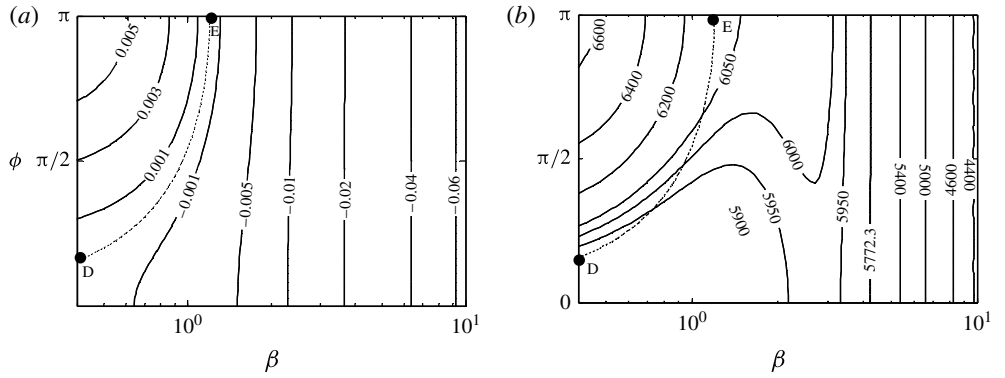

FIGURE 19. Variations of the pressure gradient correction $Re\,\mathrm{d}p_1/\mathrm{d}x$ (a) and the critical Reynolds number Re_c (b) as a function of the groove wavenumber β and the phase shift ϕ between groove systems on both walls for the channel geometry given by (4.1) with and $S_L = S_U = 0.05$. Dotted lines correspond to $Re\,\mathrm{d}p_1/\mathrm{d}x = 0$. Points D, E are located at $(\phi, \beta) = (0.167\pi, 0.4)$, $(\pi, 1.2)$, respectively.

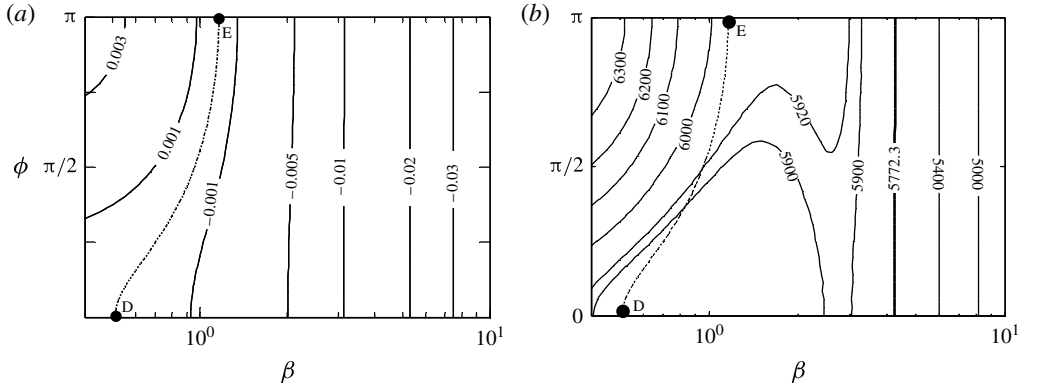

FIGURE 20. Variations of the pressure gradient correction $Re\,\mathrm{d}p_1/\mathrm{d}x$ (a) and the critical Reynolds number Re_c (b) as a function of the groove wavenumber β and the phase shift ϕ between groove systems on both walls for the channel geometry given by (4.1) $S_L = 2S_U = 0.05$. Dotted lines correspond to $Re\,\mathrm{d}p_1/\mathrm{d}x = 0$. Points D, E are located at $(\phi, \beta) = (0, 0.5)$, $(\pi, 1.1)$, respectively.

4.2. *Grooves with arbitrary shapes*

The previous section provides a detailed discussion of the instability in a channel with sinusoidal grooves. We shall now turn our attention to grooves of arbitrary shapes. Grooves with triangular, trapezoidal and rectangular shapes shown in figure 21 have been selected for the analysis. Each shape has been represented using a Fourier expansion, e.g. (2.2), which has been truncated after a finite number of terms. Neutral stability curves of the type displayed in figure 22 have been computed for each shape represented by different numbers of Fourier terms. It can be seen that Re_c determined for the triangular grooves represented using the leading term from the Fourier expansion, the first two terms, and the first three terms are nearly identical. The same conclusion applies to the trapezoidal grooves; in this case the difference between

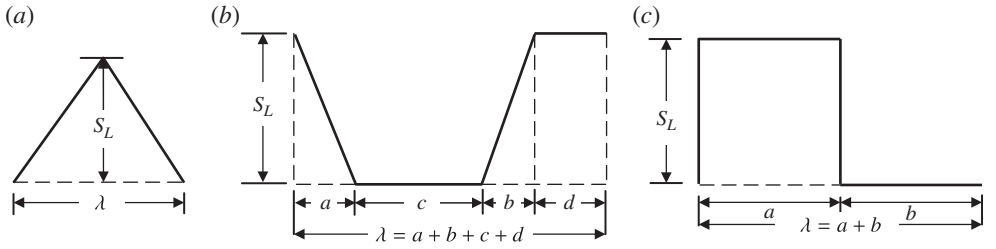

FIGURE 21. Groove shapes used in this study: (*a*) triangular groove; (*b*) trapezoidal groove; (*c*) rectangular groove. Here λ denotes the groove wavelength.

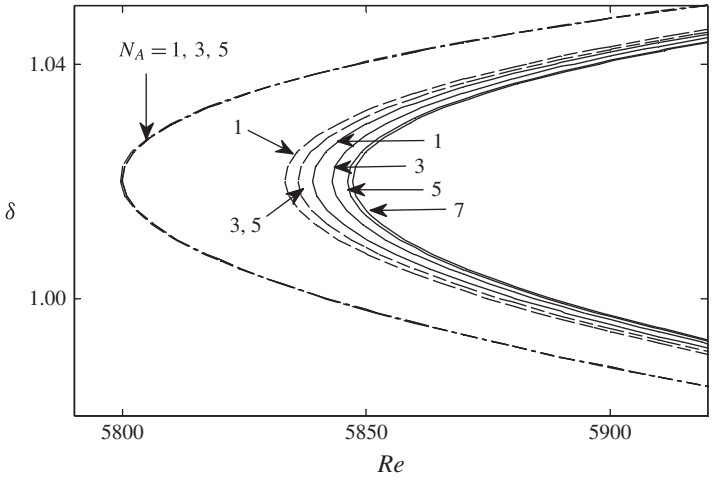

FIGURE 22. The neutral curves in the (Re, δ)-plane for flow in channels with triangular grooves (dashed-dotted lines), trapezoidal grooves (dashed lines; $a = b = \lambda/6$, $c = d = \lambda/3$, see figure 21*b* for notation), and rectangular grooves (solid lines: $a = b = \lambda/2$, see figure 21*c* for notation). All grooves have the same amplitude $S_L = 0.05$ and the same wavenumber $\beta = 1$. Their shapes are described using 1, 3, 7 leading Fourier modes from the complete Fourier expansion describing the geometry.

shapes represented by either three or five Fourier modes is negligible (the reader may note that the even terms in the Fourier expansions are zero for such shapes). It can be concluded that the difference between Re_c determined either on the basis of the shape represented by its leading Fourier mode or using the complete shape is at most 0.05 %. Rectangular grooves pose a challenge due to the existence of the Gibb's phenomenon (Wilbraham 1848; Gibbs 1898, 1899). In this case, results displayed in figure 22 demonstrate that one needs to use up to seven Fourier modes in the shape representation for the accurate determination of Re_c. Use of only one Fourier mode to represent the groove shape results in an error of Re_c not larger than 0.5 %. This demonstrates the generality of the results discussed in the previous section as the sinusoidal groove can be interpreted as representing an arbitrary groove replaced by the leading Fourier mode from its Fourier representation. The results illustrated in figure 22 form the basis of the reduced geometry model which significantly simplifies the analysis of the effects of grooves on the flow stability. There is no need to study all possible shapes as results based on the leading Fourier mode provide accuracy

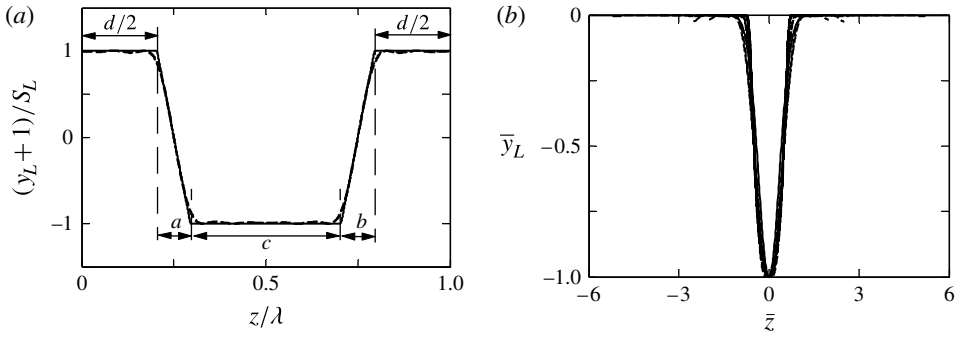

FIGURE 23. The optimal shapes for $\beta = 0.2$, 0.5 for the equal-depth (a) and the unequal-depth grooves (b) with $S_L = 0.01$, 0.03, 0.05 in the former case and $S_{L,U} = 0.01$, 0.03, 0.05 in the latter case (see the text for details). The best-fitted trapezoid ($a = b = \lambda/8$, $c = d = 3\lambda/8$) displayed in (a) overlaps with the actual grooves after all shapes had been rescaled with the groove amplitude. The universal Gaussian function $\bar{y} = -\mathrm{e}^{-4\bar{z}^2}$ displayed in (b) overlaps with the actual grooves after all shapes have been rescaled with the peak-to-bottom distance as the vertical length scale, i.e. $\bar{y}_L = (y_L + 1 - S_{L,U})/(D_{opt} + S_{L,U})$, and width at half-height W_{half} as the horizontal length scale, i.e. $\bar{z} = (z - z_0)/W_{half}$.

sufficient for most applications. The stability characteristics can be determined only once and then made available in the tabulated/graphical form, i.e. § 4.1. The above discussion also demonstrates that the stability response of the flow is insensitive to details of the groove geometry.

4.3. *Optimal grooves*

It is known that longitudinal grooves are able to significantly reduce the laminar drag if the groove wavenumber is sufficiently small; this effect occurs only for grooves with $\beta < \beta_{cr} \approx 0.965$ (see § 2.4). The best groove shape for the maximization of the drag reduction has been determined in Moradi & Floryan (2013*a*) for annular flow and by Mohammadi & Floryan (2013*b*) for planar flow. The shape of the optimal groove depends on the type of constraint. In the case of equal-depth grooves both height and depth are imposed and kept equal. In the case of the unequal-depth grooves the height is imposed while the depth is determined through the optimization process; the resulting grooves has different height and depth. In the former case, the optimal grooves are well approximated by a certain universal trapezoid (see figure 23*a*; $a = b = \lambda/8$ and $c = d = 3\lambda/8$). In the latter case, they are well approximated by a Gaussian function (see figure 23*b*; $\bar{y} = \mathrm{e}^{-4\bar{z}^2}$). It is of interest to determine the effects of such grooves on the flow stability as this would provide a limit on their applicability as drag-reducing devices. The optimization process requires access to more information about the groove geometry; the number of Fourier modes that has to be used increases to approximately 5–7 (Moradi & Floryan 2013*a*,*b*) and forms the basis for the reduced geometry model for groove optimization. In the stability analysis the optimal shapes were represented using at least ten Fourier modes in order to reduce any potential error margin.

Neutral curves in the (Re, δ)-plane for equal-depth grooves represented using the universal trapezoid are displayed in figure 24. It can be seen that such grooves stabilize the flow beyond what is possible with the sinusoidal grooves, however, the

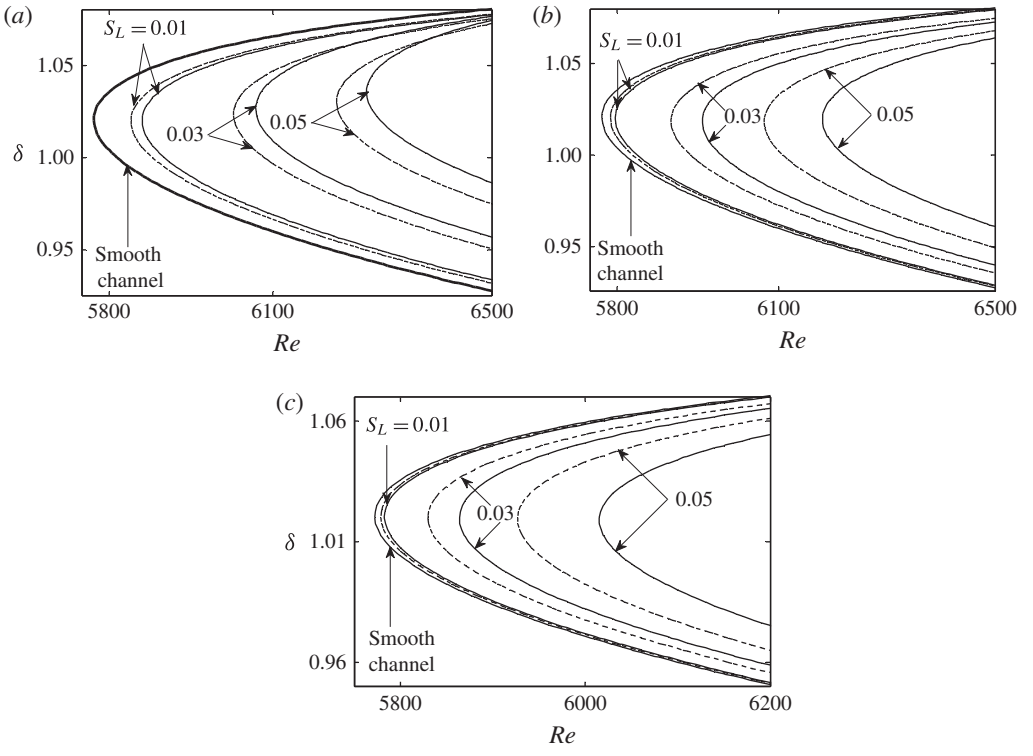

FIGURE 24. Neutral curves in the (Re, δ) plane for channel fitted with optimal, equal-depth grooves at the lower wall. The groove geometry is represented by the universal trapezoid with $a = b = \lambda/8$ and $c = d = 3\lambda/8$ (see figure 23 for notation). Results for the sinusoidal grooves are given for reference (dashed lines). Figure 24(*a–c*) provide results for the groove wavenumbers $\beta = 0.2$, 0.5 and 0.8, respectively.

corresponding increase of Re_c is fairly small. Figure 25 displays neutral curves for the unequal-depth grooves at the lower wall with heights fixed at $S_{L,U} = 0.01$, 0.03, 0.05 and depths determined by the optimization process. There are no reference curves in this figure as a single Fourier mode cannot describe such geometries. Since the optimal depth increases significantly with reduction of β and an increase of $S_{L,U}$, results are presented only for those cases where the depth did not breach the limit of 0.05 used throughout this analysis. It can be seen that the range of stabilization achieved with these grooves is similar to that found in the case of the equal-depth grooves (compare figures 24 and 25).

5. Conclusions

The analysis of the stability of the flow in a channel fitted with longitudinal grooves has been carried out. Only grooves with an amplitude less than $S = 0.05$ were considered. It is known that, in general, the effects of grooves can be divided into effects associated with a change in the mean position of the wall and effects associated with the shape-induced modulations. This analysis is focused on the modulation effects. Grooves may have an arbitrary but Fourier transformable form that does not affect the mean position of the wall. As there is an uncountable number

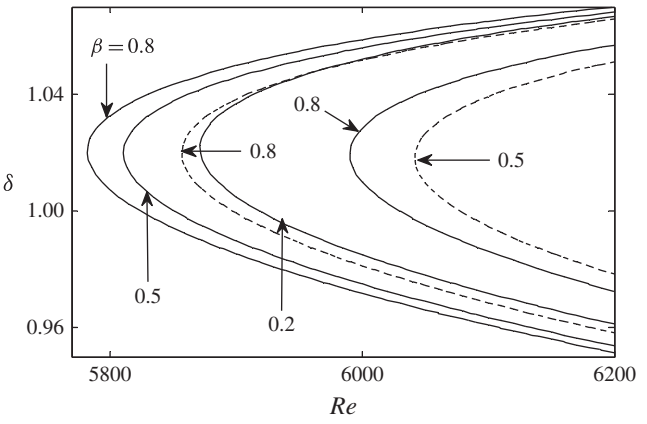

FIGURE 25. Neutral curves in the (Re, δ) plane for a channel fitted with the optimal unequal-depth grooves at the lower wall. The groove geometry is represented using the universal Gaussian function. Solid, dashed and dashed-dotted lines correspond to grooves with heights $S_{L,U} = 0.01$, 0.03 and 0.05, respectively. Results are presented only for these cases where the optimal depth has not breached the limit of 0.05 used throughout this analysis. Three curves are given for $\beta = 0.8$ ($S_{L,U} = 0.01$, 0.03, 0.05), two curves are given for $\beta = 0.5$ ($S_{L,U} = 0.01$, 0.03) and one curve is given for $\beta = 0.2$ ($S_{L,U} = 0.01$).

of possible groove shapes, the applicability of the reduced geometry concept has been investigated; it has been shown that such a model applies to the analysis of flow stability in the presence of longitudinal grooves. This model permits the replacement of an arbitrary groove with the leading term from the Fourier expansion describing its geometry. The difference between the critical Reynolds numbers determined using either the complete groove geometry or just the leading Fourier term from its Fourier representation is below 1 % for the system parameters used in this study.

A detailed analysis has been carried out for sinusoidal grooves, i.e. grooves represented by a single Fourier mode. Only disturbances corresponding to travelling waves in the limit of zero groove amplitude have been found. It is known that the two-dimensional waves play a critical role in a smooth channel. It has been shown that disturbances corresponding to the two-dimensional waves in the limit of zero groove amplitude play the critical role in the grooved channel.

The presence of grooves leads to flow stabilization for groove wavenumbers $\beta < \beta_{tran} \approx 4.22$ and flow destabilization for larger β. The destabilization is quite strong as the critical Reynolds number increases fairly rapidly with an increase of β, but stabilization associated with the reduction of β is mild. The stabilizing/destabilizing effects increase with an increase of the groove amplitude. Variations of the critical Reynolds number over the whole range of groove wavenumbers and groove amplitudes of interest have been given. Their results permit the assessment of stability properties of grooves of an arbitrary shape through invocation of the reduced geometry model.

The topology of the disturbance velocity field at the onset is highly three-dimensional. Its structure is rather simple for large β with groove effects limited to the neighbourhood of the grooved wall. Reduction of β below β_{tran} leads to large changes and increased complexity of the flow structure with groove effects visible in the whole flow domain.

Special attention has been paid to the effects of long-wavelength, drag-reducing grooves. It has been shown that such grooves lead to a small increase of the critical

Reynolds number compared with the smooth channel. The stabilizing effect has been found in the case of the optimal equal-depth grooves as well as in the case of the optimal unequal-depth grooves. It can be concluded that the use of the drag-reducing grooves does not lead to an early breakdown into turbulence and, thus, the flow should remain laminar over approximately the same range of Reynolds numbers as found in the case of smooth channel.

Acknowledgement

This work has been carried out with the support of NSERC of Canada.

Appendix A. Solution of the stationary state in the small wavenumber limit

The governing equations, the boundary conditions and the constraints forming the four leading-order systems resulting from the small-wavenumber approximation (see § 2.3):

$$O(\beta^0): \frac{\partial^2 U_0}{\partial \varsigma^2} - ReH^2 \frac{\mathrm{d}P_0}{\mathrm{d}x} = 0, \quad U_0(\chi, \pm 1) = 0, \quad \frac{1}{2\pi}\int_{\chi=0}^{\chi=2\pi}\int_{\varsigma=-1}^{\varsigma=1} HU_0 \,\mathrm{d}\varsigma \,\mathrm{d}\chi = \frac{4}{3}, \tag{A 1a–c}$$

$$O(\beta^1): \frac{\partial^2 U_1}{\partial \varsigma^2} - ReH^2 \frac{\mathrm{d}P_1}{\mathrm{d}x} = 0, \quad U_1(\chi, \pm 1) = 0, \quad \int_{\chi=0}^{\chi=2\pi}\int_{\varsigma=-1}^{\varsigma=1} HU_1 \,\mathrm{d}\varsigma \,\mathrm{d}\chi = 0, \tag{A 2a–c}$$

$$\begin{aligned} O(\beta^2): &\frac{\partial^2 U_2}{\partial \varsigma^2} - ReH^2 \frac{\mathrm{d}P_2}{\mathrm{d}x} + [2H_\chi G_\chi + 2\varsigma H_\chi^2 - H(G_{\chi\chi} + \varsigma H_{\chi\chi})]\frac{\partial U_0}{\partial \varsigma} \\ &- 2H(G_\chi + \varsigma H_\chi)\frac{\partial^2 U_0}{\partial \varsigma \partial \chi} + H^2 \frac{\partial^2 U_0}{\partial \chi^2} + ReH^2(G_\chi + \varsigma H_\chi)\frac{\mathrm{d}P_0}{\mathrm{d}x} = 0, \\ &U_2(\chi, \pm 1) = 0, \quad \int_{\chi=0}^{\chi=2\pi}\int_{\varsigma=-1}^{\varsigma=1} HU_2 \,\mathrm{d}\varsigma \,\mathrm{d}\chi = 0, \end{aligned} \tag{A 3a–c}$$

$$O(\beta^3): \frac{\partial^2 U_3}{\partial \varsigma^2} - ReH^2 \frac{\mathrm{d}P_3}{\mathrm{d}x} = 0, \quad U_3(\chi, \pm 1) = 0, \quad \int_{\chi=0}^{\chi=2\pi}\int_{\varsigma=-1}^{\varsigma=1} HU_3 \,\mathrm{d}\varsigma \,\mathrm{d}\chi = 0. \tag{A 4a–c}$$

Appendix B. Definitions of operators $T, S, C, E_v, E_\eta, H_v, H_\eta$

Here we give definitions of the operators $T, S, C, E_v, E_\eta, H_v, H_\eta$ appearing in the linear disturbance equations (see § 3.1)

$$T^{(m)}(y) = Re^{-1}(D^2 - k_m^2)^2 + \mathrm{i}(D^2 - k_m^2)[\sigma - \delta u_0(y)] + \mathrm{i}\delta D^2 u_0(y) \tag{B 1}$$

$$S^{(m)}(y) = Re^{-1}[D^2 - k_m^2 - \mathrm{i}\delta Re u_0(y) + \mathrm{i}\sigma], \tag{B 2}$$

$$C^{(m)}(y) = t_m D u_0(y) \tag{B 3}$$

$$H_v^{(m,n)}(y) = -\mathrm{i}\delta(D^2 + k_m^2)u_1^{(n)}(y) + \frac{2\mathrm{i}n\beta t_{m-n}}{k_{m-n}^2} D u_1^{(n)}(y) D + \frac{\mathrm{i}\delta}{k_{m-n}^2}[k_m^2 - (n\beta)^2]u_1^{(n)}(y)D^2, \tag{B 4}$$

$$H_{\eta}^{(m,n)}(y) = \frac{2n\beta\delta^2}{k_{m-n}^2}[Du_1^{(n)}(y) + u_1^{(n)}(y)D], \tag{B 5}$$

$$E_{v}^{(m,n)}(y) = \left[-t_m Du_1^{(n)}(y) + n\beta\left(1 + \frac{n\beta t_{m-n}}{k_{m-n}^2}\right)u_1^{(n)}(y)D\right], \tag{B 6}$$

$$E_{\eta}^{(m,n)}(y) = \mathrm{i}\delta\left(1 - \frac{n^2\beta^2}{k_{m-n}^2}\right)u_1^{(n)}(y), \tag{B 7}$$

$$t_m = \mu + m\beta, \quad k_m^2 = \delta^2 + t_m^2, \tag{B 8a,b}$$

where $D^n = \mathrm{d}^n/\mathrm{d}y^n$.

Appendix C. Discretization of the disturbance equations

The flow domain is contained between $(-1 - y_b)$ and $(1 + y_t)$, where y_b and y_t denote locations of the groove extremities. In order to use the standard definition of the Chebyshev polynomials, this domain is mapped into $(-1, 1)$ using a transformation of the form

$$\hat{y} = [y - (1 + y_t)]\Gamma + 1, \quad \Gamma = 2(2 + y_t + y_b)^{-1}. \tag{C 1}$$

The T, S, C, E_v, E_η, H_v, H_η operators in the new coordinate system take the form

$$T^{(m)}(\hat{y}) = Re^{-1}(\Gamma^2D^2 - k_m^2)^2 + \mathrm{i}(\Gamma^2D^2 - k_m^2)[\sigma - \delta u_0(\hat{y})] + \mathrm{i}\delta\Gamma^2D^2u_0(\hat{y}) \tag{C 2}$$

$$S^{(m)}(\hat{y}) = Re^{-1}[\Gamma^2D^2 - k_m^2 - \mathrm{i}\delta Reu_0(\hat{y}) + \mathrm{i}\sigma], \tag{C 3}$$

$$C^{(m)}(\hat{y}) = t_m\Gamma Du_0(\hat{y}) \tag{C 4}$$

$$H_{v}^{(m,n)}(\hat{y}) = -\mathrm{i}\delta(\Gamma^2D^2 + k_m^2)u_1^{(n)}(\hat{y}) + \frac{2\mathrm{i}n\beta t_{m-n}\Gamma^2}{k_{m-n}^2}Du_1^{(n)}(\hat{y})D + \frac{\mathrm{i}\delta\Gamma^2}{k_{m-n}^2}[k_m^2 - (n\beta)^2]u_1^{(n)}(\hat{y})D^2, \tag{C 5}$$

$$H_{\eta}^{(m,n)}(\hat{y}) = \frac{2n\beta\delta^2\Gamma}{k_{m-n}^2}[Du_1^{(n)}(\hat{y}) + u_1^{(n)}(\hat{y})D], \tag{C 6}$$

$$E_{v}^{(m,n)}(\hat{y}) = \Gamma\left[-t_m Du_1^{(n)}(\hat{y}) + n\beta\left(1 + \frac{n\beta t_{m-n}}{k_{m-n}^2}\right)u_1^{(n)}(\hat{y})D\right] \tag{C 7}$$

$$E_{\eta}^{(m,n)}(\hat{y}) = \mathrm{i}\delta\left(1 - \frac{n^2\beta^2}{k_{m-n}^2}\right)u_1^{(n)}(\hat{y}). \tag{C 8}$$

The unknown modal functions are expressed as Chebyshev expansions (3.9) and the mean flow and the reference flow quantities are expressed in terms of the relevant Chebyshev expansions of the form

$$u_1^{(n)}(\hat{y}) = \sum_{k=0}^{N_T} G_{l,B}^{(n)}T_k(\hat{y}), \tag{C 9}$$

$$\left.\begin{aligned} u_0(\hat{y}) &= -T_2(\hat{y})/(2\Gamma^2) - 2\,(1 + y_t - 1/\Gamma)\,T_1(\hat{y})/\Gamma \\ &\quad + \left[1 - (1 + y_t - 1/\Gamma)^2 - 1/(2\Gamma^2)\right]T_0(\hat{y}), \\ Du_0(\hat{y}) &= -2T_1(\hat{y})/(\Gamma^2) - 2(1 + y_t - 1/\Gamma)T_0(\hat{y})/\Gamma, \\ D^2u_0(\hat{y}) &= -2T_0(\hat{y})/\Gamma^2. \end{aligned}\right\} \tag{C 10}$$

Substitution of (C 9) and (C 10) into (C 2)–(C 8) results in an algebraic system of the form

$$\sum_{k=0}^{N_T}\left\{Re^{-1}\Gamma^4 D^4 T_k-\Gamma^2(2Re^{-1}k_m^2+\mathrm{i}\delta u_0)D^2T_k+\left[Re^{-1}k_m^4+\mathrm{i}\delta\left(\Gamma^2D^2u_0+k_m^2u_0\right)\right]T_k\right\}G_{k,v}^{(m)}-\sum_{n=-N_N}^{+N_N}\sum_{k=0}^{+N_T}[H_v^{(m,n)}T_kG_{k,v}^{(m-n)}+H_\eta^{(m,n)}T_kG_{k,\eta}^{(m-n)}]=-\mathrm{i}\sigma\sum_{k=0}^{+N_T}(\Gamma^2D^2T_k-k_m^2T_k)G_{k,v}^{(m)},\tag{C 11a}$$

$$\sum_{k=0}^{N_T}[Re^{-1}\Gamma^2D^2T_k-(Re^{-1}k_m^2+\mathrm{i}\delta u_0)T_k]G_{k,\eta}^{(m)}+t_m\Gamma Du_0T_kG_{k,v}^{(m)}-\sum_{n=-N_N}^{+N_N}\sum_{k=0}^{+N_T}[E_v^{(m,n)}T_kG_{k,v}^{(m-n)}+E_\eta^{(m,n)}T_kG_{k,\eta}^{(m-n)}]=-\mathrm{i}\sigma\sum_{k=0}^{+N_T}T_kG_{k,\eta}^{(m)}.\tag{C 11b}$$

Application of the Galerkin projection method leads to a linear system for the expansion coefficients of the form

$$\sum_{k=0}^{N_T}\left[Re^{-1}\Gamma^4\langle T_j,D^4T_k\rangle-2Re^{-1}k_m^2\Gamma^2\langle T_j,D^2T_k\rangle+Re^{-1}k_m^4\langle T_j,T_k\rangle-\mathrm{i}\delta\Gamma^2\langle T_j,u_0D^2T_k\rangle+\mathrm{i}\delta k_m^2\langle T_j,u_0T_k\rangle+\mathrm{i}\delta\Gamma^2\langle T_j,D^2u_0T_k\rangle\right]G_{k,v}^{(m)}+\sum_{n=-N_N}^{N_N}\sum_{l=0}^{N_T}\left[\mathrm{i}\delta k_m^2\langle T_j,T_lT_k\rangle+\mathrm{i}\delta\Gamma^2\langle T_j,D^2T_lT_k\rangle-\frac{2\mathrm{i}n\beta\delta t_{m-n}\Gamma^2}{k_{m-n}^2}\langle T_j,DT_lDT_k\rangle-\frac{\mathrm{i}\delta\Gamma^2(k_m^2-n^2\beta^2)}{k_{m-n}^2}\langle T_j,T_lD^2T_k\rangle\right]G_{l,B}^{(n)}G_{k,v}^{(m-n)}-\sum_{n=-N_N}^{N_N}\sum_{l=0}^{N_T}\frac{2n\beta\delta^2\Gamma}{k_{m-n}^2}\left(\langle T_j,DT_lT_k\rangle+\langle T_j,T_lDT_k\rangle\right)G_{l,B}^{(n)}G_{k,\eta}^{(m-n)}=-\mathrm{i}\sigma\left(\Gamma^2\langle T_j,D^2T_k\rangle-k_m^2\langle T_j,T_k\rangle\right)G_{k,v}^{(m)},\tag{C 12a}$$

$$\sum_{k=0}^{N_T}\left[Re^{-1}\Gamma^2\langle T_j,D^2T_k\rangle-Re^{-1}k_m^2\langle T_j,T_k\rangle-\mathrm{i}\delta\langle T_j,u_0T_k\rangle\right]G_{k,\eta}^{(m)}+t_m\Gamma\langle T_j,Du_0T_k\rangle G_{k,v}^{(m)}+\sum_{n=-N_N}^{N_N}\sum_{l=0}^{N_T}\left[t_m\Gamma\langle T_j,DT_lT_k\rangle-n\beta\Gamma\left(1+\frac{n\beta t_{m-n}}{k_{m-n}^2}\right)\langle T_j,T_lDT_k\rangle\right]G_{l,B}^{(n)}G_{k,v}^{(m-n)}+\sum_{n=-N_N}^{N_N}\sum_{l=0}^{N_T}\mathrm{i}\delta\left(\frac{n^2\beta^2}{k_{m-n}^2}-1\right)\langle T_j,T_lT_k\rangle G_{l,B}^{(n)}G_{k,\eta}^{(m-n)}=-\mathrm{i}\sigma\langle T_j,T_k\rangle G_{k,\eta}^{(m)}.\tag{C 12b}$$

The inner product $\langle T_j, D^nT_lD^mT_k\rangle$ is defined as

$$\langle T_j,D^nT_lD^mT_k\rangle=\int_{-1}^{1}T_j(\hat{y})D^nT_l(\hat{y})D^mT_k(\hat{y})\omega(\hat{y})\,\mathrm{d}\hat{y},\tag{C 13}$$

where $\omega(y) = 1/\sqrt{1-y^2}$. Evaluation of these products can be simplified by taking advantage of the orthogonality properties of the Chebyshev polynomials (See appendix A).

Appendix D. Description of boundary relations required to complete formulation of the linear stability problem

The homogeneous boundary conditions (3.4) need to be expressed in terms of $\eta^{(m)}(\hat{y})$ and $g_v^{(m)}(\hat{y})$. They can be written for the lower wall in the form

$$u_D(x,\hat{y}_L,z,t) = \sum_{n=-N_N}^{+N_N}\left[\frac{\mathrm{i}\delta\Gamma}{k_n^2}Dg_v^{(n)}(\hat{y}_L) - \frac{t_n}{k_n^2}\eta^{(n)}(\hat{y}_L)\right]\mathrm{e}^{\mathrm{i}[\delta x+(\mu+n\beta)z-\sigma t]} = 0, \tag{D 1}$$

$$v_D(x,\hat{y}_L,z,t) = \sum_{n=-N_N}^{+N_N} g_v^{(n)}(\hat{y}_L)\mathrm{e}^{\mathrm{i}[\delta x+(\mu+n\beta)z-\sigma t]} = 0, \tag{D 2}$$

$$w_D(x,\hat{y}_L,z,t) = \sum_{n=-N_N}^{+N_N}\left[\frac{\mathrm{i}t_n\Gamma}{k_n^2}Dg_v^{(n)}(\hat{y}_L) + \frac{\delta}{k_n^2}\eta^{(n)}(\hat{y}_L)\right]\mathrm{e}^{\mathrm{i}[\delta x+(\mu+n\beta)z-\sigma t]} = 0. \tag{D 3}$$

The location of this wall is given as

$$\hat{y}_L(z) = \sum_{n=-N_A}^{N_A} A_L^{(n)}\mathrm{e}^{\mathrm{i}n\beta z} \tag{D 4}$$

where $A_L^{(n)} = -\Gamma(2+y_t-H_L^{(n)})+1$ for $n=0$ and $A_L^{(n)} = \Gamma H_L^{(n)}$ for $n\neq 0$. As the first step, consider boundary condition (D 1). Substitution of (3.9) into (D 1) leads to

$$\sum_{n=-N_N}^{+N_N}\sum_{k=0}^{+N_T}\frac{\mathrm{i}\delta\Gamma}{k_n^2}DT_k(\hat{y}_L(z))G_{k,v}^{(n)}\mathrm{e}^{\mathrm{i}[\delta x+(\mu+n\beta)z-\sigma t]} - \sum_{n=-N_N}^{+N_N}\sum_{k=0}^{+N_T}\frac{t_n}{k_n^2}T_k(\hat{y}_L(z))G_{k,\eta}^{(n)}\mathrm{e}^{\mathrm{i}[\delta x+(\mu+n\beta)z-\sigma t]} = 0. \tag{D 5}$$

Values of the Chebyshev polynomials and their first derivatives along the wall appearing in the above relation i.e. $T_k(\hat{y}_L(z))$ and $DT_k(\hat{y}_L(z))$, represent periodic functions of z and, thus, can be expressed using Fourier expansions of the form

$$T_k(\hat{y}_L(z)) = \sum_{m=-\infty}^{+\infty}(w_L)_k^{(m)}\mathrm{e}^{\mathrm{i}m\beta z}, \quad DT_k(\hat{y}_L(z)) = \sum_{m=-\infty}^{+\infty}(d_L)_k^{(m)}\mathrm{e}^{\mathrm{i}m\beta z}. \tag{D 6a,b}$$

The reader may note that substitution of (D 6) into (D 5) leads to a certain Fourier expansion whose convergence rate affects the number of Fourier modes that have to be used in the solution. The expansion has, in general, a different convergence rate from expansion (3.7).

Evaluation of coefficients $(w_L)_k^{(m)}$ begins with the lowest-order Chebyshev polynomial, i.e.

$$T_0 = 1 \Longrightarrow \sum_{m=-\infty}^{+\infty} w_{L,0}^{(m)}\mathrm{e}^{\mathrm{i}m\beta z} = 1 \Longrightarrow \begin{cases} w_{L,0}^{(0)} = 1 \\ w_{L,0}^{(m)} = 0, \quad m\neq 0, \end{cases} \tag{D 7}$$

$$T_1\left[\hat{y}_L(z)\right]=\hat{y}_L(z)\Longrightarrow\sum_{m=-\infty}^{+\infty}w_{L,1}^{(m)}\mathrm{e}^{\mathrm{i}m\beta z}=\sum_{m=-\infty}^{+\infty}A_L^{(m)}\mathrm{e}^{\mathrm{i}m\beta z}\Longrightarrow w_{L,1}^{(m)}=A_L^{(m)}. \tag{D 8}$$

The remaining coefficients $w_{L,k}^{(m)}$ $(k\geqslant 2)$ can be computed using the Chebyshev recursion relation which results in

$$w_{L,k+1}^{(m)}=2\sum_{n=-N_A}^{N_A}A_L^{(n)}w_{L,k}^{(m-n)}-w_{L,k-1}^{(m)},\quad k\geqslant 2. \tag{D 9}$$

Evaluation of the coefficients $(d_L)_k^{(m)}$ also begins with the lowest-order polynomial, i.e.

$$DT_0=0\Longrightarrow\sum_{m=-\infty}^{+\infty}d_{L,0}^{(m)}\mathrm{e}^{\mathrm{i}m\beta z}=0\Longrightarrow d_{L,0}^{(0)}=0, \tag{D 10}$$

$$DT_1=1\Longrightarrow\sum_{m=-\infty}^{+\infty}d_{L,0}^{(m)}\mathrm{e}^{\mathrm{i}m\beta z}=1\Longrightarrow\begin{cases}d_{L,0}^{(0)}=1\\ d_{L,0}^{(m)}=0,\quad m\neq 0,\end{cases} \tag{D 11}$$

$$DT_2\left[\hat{y}_L(z)\right]=4\hat{y}_L(z)\Longrightarrow\sum_{m=-\infty}^{+\infty}d_{L,2}^{(m)}\mathrm{e}^{\mathrm{i}m\beta z}=\sum_{m=-\infty}^{+\infty}4A_L^{(m)}\mathrm{e}^{\mathrm{i}m\beta z}\Longrightarrow d_{in,2}^{(m)}=4A_{in}^{(m)}. \tag{D 12}$$

The remaining coefficients $d_{L,k}^{(m)}$, $k\geqslant 3$ can be computed using the Chebyshev recursive formula and have the following form

$$d_{L,k+1}^{(m)}=2\sum_{n=-N_A}^{N_A}A_L^{(n)}d_{L,k}^{(m-n)}-d_{L,k-1}^{(m)}-w_{L,k}^{(m)},\quad k\geqslant 3. \tag{D 13}$$

Substitution of (D 6) into (D 5) and separation of Fourier modes lead to a boundary relation of the form

$$\sum_{n=-N_N}^{+N_N}\sum_{k=0}^{+N_T}\frac{\mathrm{i}\delta\Gamma}{k_m^2}(d_L)_k^{(n-m)}G_{k,v}^{(n)}-\sum_{n=-N_N}^{+N_N}\sum_{k=0}^{+N_T}\frac{t_m}{k_m^2}(w_L)_k^{(n-m)}G_{k,\eta}^{(n)}=0 \tag{D 14}$$

which expresses condition (D 1). Following the same procedure, the boundary conditions for v_D and w_D can be written in the form

$$\sum_{n=-N_N}^{+N_N}\sum_{k=0}^{+N_T}(w_L)_k^{(n-m)}G_{k,v}^{(n)}=0. \tag{D 15}$$

$$\sum_{n=-N_N}^{+N_N}\sum_{k=0}^{+N_T}\frac{\mathrm{i}t_m\Gamma}{k_m^2}(d_L)_k^{(n-m)}G_{k,v}^{(n)}+\sum_{n=-N_N}^{+N_N}\sum_{k=0}^{+N_T}\frac{\delta}{k_m^2}(w_L)_k^{(n-m)}G_{k,\eta}^{(n)}=0. \tag{D 16}$$

Boundary relations for the upper wall can be obtained by simply changing subscript 'L' into 'U' in the above equations. These relations provide the groove-induced coupling between different Fourier modes. The other coupling is provided by the field equations (3.8).

In general, the total number of available boundary relations is $N_N + N_T N_A$, where N_N is the number of Fourier modes used in the discretization of the field equations, N_T is the number of the Chebyshev polynomials used in the discretization of the modal functions and N_A denotes the number of Fourier modes used to describe the groove geometry. Since only N_N modes are used in the numerical solution, one can enforce only N_N of these conditions. The remaining conditions can either be used *a posteriori* as a convenient test for the consistency of the algorithm or can be utilized directly leading to the over-determined formulation (Husain *et al.* 2009).

REFERENCES

Asai, M. & Floryan, J. M. 2006 Experiments on the linear instability of flow in a wavy channel. *Eur. J. Mech. (*B*/Fluids)* **25**, 971–986.

Bloch, F. 1928 Über die Quantenmechanik der Elektronen in Kristallgittern. *Z. Phys.* **52**, 555–600.

Boiko, A. V., Jung, K. H., Chun, H. H. & Lee, I. 2007 Effect of riblets on the streaky structures excited by free stream tip vortices in boundary layer. *J. Mech. Sci. Engng* **21**, 196–206.

Boiko, A. V., Kozlov, V. V., Syzrantsev, V. V. & Scherbakov, V. A. 1997 Transition control by riblets in swept wing boundary layer with embedded streamwise vortex. *Eur. J. Mech. (*B*/Fluids)* **16**, 465–482.

Boiko, A. V. & Nechepurenko, Yu. M. 2010 Technique for the numerical analysis of the riblet effect on temporal stability of plane flows. *Comput. Math. & Math. Phys.* **50**, 1055–1070.

Cabal, A., Szumbarski, J. & Floryan, J. M. 2001 Numerical simulation of flows over corrugated walls. *Comput. Fluids* **30**, 753–776.

Cabal, T., Szumbarski, J. & Floryan, J. M. 2002 Stability of flow in a wavy channel. *J. Fluid Mech.* **457**, 191–212.

Canuto, C., Hussaini, M. Y., Quarteroni, A. & Zang, T. A. 2006 *Spectral Methods. Fundamentals in Single Domains*. Springer.

Coddington, E. A. & Levinson, N. 1965 *Theory of Ordinary Differential Equations*. McGraw-Hill.

Darcy, H. 1857 *Recherches Expérimentales Relatives au Mouvement de l'eau Dans les Tuyaux*. Mallet-Bachelier.

Dean, B. & Bhushan, B. 2010 Shark-skin surfaces for fluid-drag reduction in turbulent flow: a review. *Phil. Trans. R. Soc.* A **368**, 4775–4806.

Denissen, N. A. & White, E. B. 2009 Continuous spectrum analysis of roughness-induced transient growth. *Phys. Fluids* **21**, 114115.

Ehrenstein, U. 1996 On the linear stability of channel flow over riblets. *Phys. Fluids* **8**, 3194–3196.

Floryan, J. M. 1997 Stability of wall-bounded shear layers in the presence of simulated distributed surface roughness. *J. Fluid Mech.* **335**, 29–55.

Floryan, J. M. 2002 Centrifugal instability of Couette flow over a wavy-wall. *Phys. Fluids* **14**, 312–322.

Floryan, J. M. 2003 Vortex instability in a diverging–converging channel. *J. Fluid Mech.* **482**, 17–50.

Floryan, J. M. 2005 Two-dimensional instability of flow in a rough channel. *Phys. Fluids* **17**, 044101.

Floryan, J. M. 2007 Three-dimensional instabilities of laminar flow in a rough channel and the concept of hydraulically smooth wall. *Eur. J. Mech. (*B*/Fluids)* **26**, 305–329.

Floryan, J. M. & Asai, M. 2011 On the transition between distributed and isolated surface roughness and its effect on the stability of channel flow. *Phys. Fluids* **23**, 104101.

Floryan, J. M. & Floryan, C. 2010 Travelling wave instability in a diverging–converging channel. *Fluid Dyn. Res.* **42**, 025509.

Gibbs, J. W. 1898 Fourier's series. *Nature* **59** (1522), 200.

Gibbs, J. W. 1899 Fourier's series. *Nature* **59** (1539), 606.

GREK, G. R., KOZLOV, V. V. & TITARENKO, S. V. 1996 An experimental study of the influence of riblets on transition. *J. Fluid Mech.* **315**, 31–45.

HAGEN, G. 1854 *Uber den Einfluss der Temperatur auf die Bewegung des Wasser in Röhren. (Mathematische Abhandhmgen)*, pp. 17–98. Akademie der Wissenschaften zu Berlin.

HERBERT, T. 1977 Finite amplitude stability of plane parallel flows. *AGARD Conference Proceedings* **224**, 3.1–3.10.

HERWIG, H., GLOSS, D. & WENTERODT, T. 2008 A new approach to understanding and modelling the influence of wall roughness on friction factors for pipe and channel flows. *J. Fluid Mech.* **613**, 35–53.

HUSAIN, S. Z. & FLORYAN, J. M. 2010 Spectrally-accurate algorithm for moving boundary problems for the Navier–Stokes equations. *J. Comput. Phys.* **229**, 2287–2313.

HUSAIN, S. Z., FLORYAN, J. M. & SZUMBARSKI, J. 2009 Over-determined formulation of the immersed boundary condition method. *Comput. Meth. Appl. Mech. Engng* **199**, 94–112.

INASAWA, A., FLORYAN, J. M. & ASAI, M. 2014 Flow recovery downstream from a surface protuberance. *Theor. Comput. Fluid Dyn.* **28**, 427–447.

JIMENEZ, J. 2004 Turbulent flows over rough walls. *Annu. Rev. Fluid Mech.* **36**, 173–196.

JIN, Y. & HERWIG, H. 2014 Turbulent flow and heat transfer in channels with shark skin surfaces: entropy generation and its physical significance. *Intl J. Heat Mass Transfer* **70**, 10–22.

KLAMP, S., MEINKE, M. & SCHRÖDER, W. 2010 Numerical simulation of riblet controlled spatial transition in a zero-pressure-gradient boundary layer. *Flow Turbul. Combust.* **85**, 57–71.

LUCHINI, P. & TROMBETTA, G. 1995 Effects of riblets upon flow stability. *Appl. Sci. Res.* **54**, 313–321.

MOHAMMADI, A. & FLORYAN, J. M. 2012 Spectral algorithm for the analysis of flows in grooved channels. *Intl J. Numer. Meth. Fluids* **69**, 606–638.

MOHAMMADI, A. & FLORYAN, J. M. 2013*a* Groove optimization for drag reduction. *Phys. Fluids* **25**, 113601.

MOHAMMADI, A. & FLORYAN, J. M. 2013*b* Pressure losses in grooved channels. *J. Fluid Mech.* **725**, 23–54.

MOODY, L. F. & PRINCETON, N. J. 1944 Friction factors for pipe flow. *Trans. ASME* **66**, 671–684.

MORADI, H. V. & FLORYAN, J. M. 2012 Algorithm for analysis of flows in ribbed annuli. *Intl J. Numer. Meth. Fluids* **68**, 805–838.

MORADI, H. & FLORYAN, J. M. 2013*a* Flows in annuli with longitudinal grooves. *J. Fluid Mech.* **716**, 280–315.

MORADI, H. & FLORYAN, J. M. 2013*b* Maximization of heat transfer across micro-channels. *Intl J. Heat Mass Transfer* **66**, 517–530.

MORKOVIN, M. V. 1990 On roughness-induced transition: facts, views and speculations. In *Instability and Transition* (ed. M. Y. Hussaini & R. G. Voigt), ICASE/NASA LARC Series, vol. 1, pp. 281–295. Springer, New York.

ORSZAG, S. A. 1971 Accurate solutions of the Orr–Sommerfeld stability equation. *J. Fluid Mech.* **50**, 689–704.

ORSZAG, S. A. & PATERA, A. T. 1983 Secondary instability of wall-bounded shear flows. *J. Fluid Mech.* **128**, 347–385.

REYNOLDS, O. 1883 An experimental investigation of the circumstances which determine whether the motion of water shall be direct or sinuous, and of the wall of resistance in parallel channels. *Phil. Trans. R. Soc. Lond.* **174**, 935–982.

ROTHENFLUE, J. A. & KING, P. I. 1995 Vortex development over flat plate riblets in a transitioning boundary layer. *AIAA J.* **33**, 1525–1526.

SAAD, Y. 2003 *Iterative Methods for Sparse Linear Systems*. SIAM.

SCHLICHTING, H. 1979 *Boundary Layer Theory*, 7th edn. McGraw-Hill.

SQUIRE, H. B. 1933 On the stability of three-dimensional distribution of viscous fluid between parallel walls. *Proc. R. Soc. Lond.* A **142**, 621–628.

SZUMBARSKI, J. 2007 Instability of viscous incompressible flow in a channel with transversely corrugated walls. *J. Theor. Appl. Mech.* **45**, 659–683.

SZUMBARSKI, J. & FLORYAN, J. M. 1999 A direct spectral method for determination of flows over corrugated boundaries. *J. Comput. Phys.* **153**, 378–402.

SZUMBARSKI, J. & FLORYAN, J. M. 2006 Transient disturbance growth in a corrugated channel. *J. Fluid Mech.* **568**, 243–272.

WALSH, M. J. 1983 Riblets as a viscous drag reduction technique. *AIAA J.* **21**, 485–486.

WHITE, E. B., RICE, J. M. & ERGIN, F. G. 2005 Receptivity of stationary transient disturbances to surface roughness. *Phys. Fluids* **17**, 064109.

WILBRAHAM, H. 1848 On a certain periodic function. *Cambridge Dublin Math. J.* **3**, 198–201.